Chapter 4
The Photosphere and Sunspots

4.1 Solar Diameter and Oblateness

Recent debates about the accuracy of measuring the solar radius attribute an uncertainty (including systematic errors) of about $\sigma_R \pm 500$ km (e.g., Emilio et al. 2012), which amounts to a relative accuracy of $\sigma_R/R \approx 0.0007$. Space-based observations are considered to be more accurate than ground-based measurements, which are impacted by the seeing through the Earth atmosphere. Celestial mechanics is known to such a high degree of precision that the exact timing of a Venus or Mercury transit is well-known. The transits can be used to improve the errors of the plate scale of instruments like the *Helioseismic and Magnetic Imager (HMI)* onboard SDO, but also to accurately determine the solar radius at a specific instrument wavelength. The basic idea is to time the instant at which the planet enters (ingression) and exits (egression) the solar disk. A comparison between the measured transit duration and the duration predicted by the ephemeris as a function of the solar radius returns the exact value of this radius.

Recent space-based measurements have been conducted with the *Michelson Doppler Imager (MDI)* onboard the SOHO during the Mercury 2003 May 7 and 2006 November 8 transits (Emilio et al. 2012). From the MDI transit data, a solar radius of $960.12'' \pm 0.09''(696, 342 \pm 65$ km) was established. This value is consistent between the transits and consistent between different MDI focus settings after accounting for systematic effects. The total transit time was obtained with an accuracy of 4 s in 2003 and 1 s in 2006. The correction ΔR to a previous nominal value of the radius $R_\odot = 696, 000 \pm 40$ km) is calculated from,

$$\Delta R = \frac{\omega^2}{R_\odot} T \ \Delta T_{OC} \ , \tag{4.1.1}$$

where ω is the speed of Mercury relative to the Sun, T is the total length of the transit, and ΔT_{OC} is the difference between the observed and ephemeris duration of

M. J. Aschwanden, *New Millennium Solar Physics*, Astrophysics and Space Science Library 458, https://doi.org/10.1007/978-3-030-13956-8_4

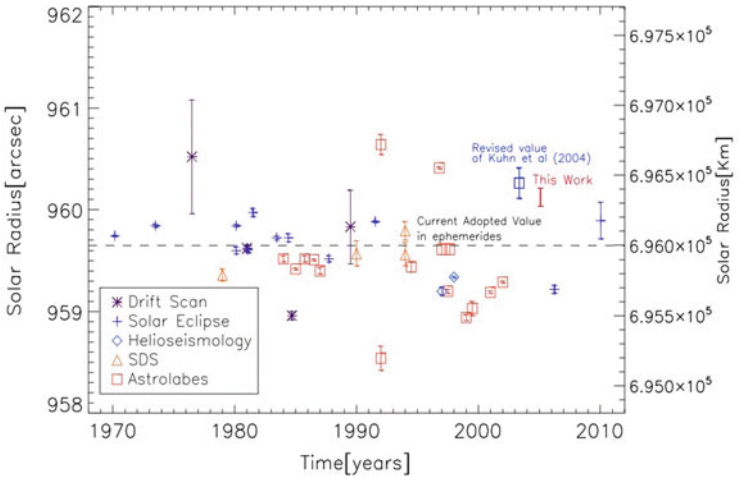

Fig. 4.1 Published measurements of the solar radius during 1970–2012, including methods such as drift scans, solar eclipses, helioseismology, *solar diameter sextant (SDS)* experiment, and astrolabe measurements. Astrolabe measurements are corrected for atmospheric and instrumental systematic effects. For references see Fig. 1 in Emilio et al. (2012)

the transit. No significant variation of the solar radius was observed over the 3 years between the two (2003, 2006) Mercury transits. A compilation of previous solar diameter measurements is shown in Fig. 4.1. Another Mercury transit was observed on 2016 May 9 with both the MDI/SOHO and HMI/SDO instruments, but the degradation of the MDI front window (which causes scattered light) and different orbits and transit paths prevented an accurate dual solar diameter measurement. The next Mercury transit will occur on 2019 November 11.

Another rare opportunity was the Venus transit on 2012 June 5 (Fig. 4.2). Venus crossings occur in two events separated by 8 years (such as on 2004 June 8 and 2012 June 5), but repeat only after 121.5 and 105.5 yrs. HMI/SDO observed the 2012 Venus transit, being the last one during this century (Emilio et al. 2015). The data have been corrected for the instrumental distortion, the point-spread function, and different background thresholds, using the information documented in Wachter et al. (2012). The obtained result is a solar radius of $959.57'' \pm 0.02$ (695, 946 ± 15 km), which is $0.55''$ smaller than the MDI result during the Mercury transit ($960.12''$), while the total uncertainty is estimated to be $0.27''$. At the same time, the Venus transit was observed with AIA, from which a solar radius of $963.04'' \pm 0.04''$ at 1600 Å, and $961.76'' \pm 0.03''$ at 1700 Å was obtained. The "visual" solar diameter depends on the wavelength (Rozelot et al. 2015). The "standard" solar radius (such as used for solar model calibrations), adopted by the IAU in 2015, was calculated using helioseismology measurements.[1] Recent measurements showed that it varies by 1–2 km during the solar cycle (Kosovichev and Rozelot 2018a).

[1] https://en.wikipedia.org/wiki/Solar_radius.

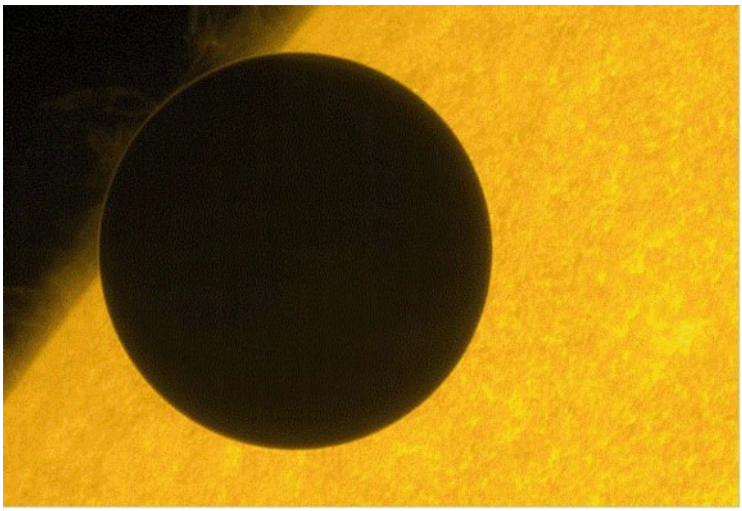

Fig. 4.2 Venus transit on 2012 June 5, observed with SOT/Hinode. Venus has a radius of 6051.8 km (Credit: Hinode Team)

Let us now turn from the solar diameter measurement to the solar oblateness measurement, which is the ratio between the equatorial and polar radius. Recent reviews about this topic can be found in Damiani et al. (2011) and Rozelot et al. (2015). Theoretically, the oblateness and centrifugal force would diminish the equatorial gravity compared to the polar gravity. The Earth has an oblateness of 1/298. The shape of the Sun is influenced by its internal rotation and the magnetic and fluid-flow stresses. The surface rotation rate, $v \approx 2$ km s^{-1} at the equator, predicts an oblateness (equator-pole radius difference) of 7.8 milli-arcsec, or $\approx 10^{-5}$. Observations with RHESSI revealed an unexpected larger flattening (Fig. 4.3) of 10.77 ± 0.44 milli arcsec (Fivian et al. 2008). The position of the limb correlates with the EUV 284 Å brightness of magnetic elements in the enhanced network, which can be used to correct for this systematic error, yielding a corrected oblateness of the non-magnetic Sun of 8.01 ± 0.14 milli arcsec, close to the theoretically expected value from rotation (Fivian et al. 2008).

According to Kuhn et al. (2012), the expected deviation of the solar-limb shape from a perfect circle is very small, but measurable with present instrumentation such as MDI/SOHO and HMI/SDO. Long-term measurements with MDI reveal that the Sun's oblate shape is distinctly constant and almost unaffected by the solar-cycle variability. Kuhn et al. (2012) find that the observed oblateness is significantly lower than theoretically expected, but by an amount that could be explained by a slower differential rotation in the outer few percent of the Sun. However, the most recent helioseismic measurements reveal rotation and asphericity variations in the near-surface shear layer during a solar cycle (Kosovichev and Rozelot 2018b).

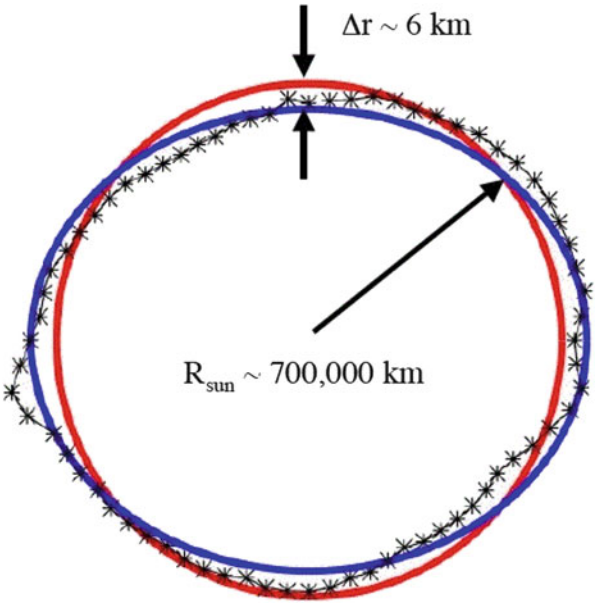

Fig. 4.3 The diagram depicts the Sun's oblateness, which is magnified by a factor of 10^4. The blue curve traces the Sun's shape averaged over a 3-month period. The black curve with asterisks traces a shorter 10-day average. The wiggles in the 10-day curve are correlated with strong magnetic ridges in the vicinity of sunspots. The red circle corresponds to a perfect sphere (Fivian et al. 2008)

How oblate is the Sun? Douglas Gough (2012) gives us the following answer: Le Verrier realized the unexplained perihelion precession of Mercury. Newcomb pointed out that this residual precession could be due to the oblateness of the Sun. Einstein demonstrated that the general theory of relativity explained almost all of the $43''$ per century perihelion precession of Mercury, assuming that the Sun is perfectly spherical without oblateness. Only 0.2% of the original discrepancy then remained to be explained otherwise, presumably by oblateness caused by the solar rotation. Gough (2012) suggests that turbulent stresses from convection could possibly contribute. Nevertheless, the analysis of HMI data (Kuhn et al. 2012) yields a too low oblateness and the conundrum remains: Why does the Sun appear to be so round?

4.2 Magnetic Flux Distribution

Although the global magnetic field of the Sun is roughly described by a poloidal dipole field during the minimum of the solar activity cycle, and with a toroidal field during the maximum, the distribution of the magnetic flux on the solar surface is much more complex. It is common practice to subdivide it into active regions

with sunspots (where the magnetic field is strongest and has mostly a closed-field configuration), Quiet Sun regions (where the field is weaker but still closed), and coronal hole regions (where the field is weak and has an open-field configuration by definition). The strongest fields are found in sunspots and amount to field strengths of $B \approx 1000$–6250 G (Okamoto and Sakurai 2018), while the weakest fields have field strengths of $B \approx 5$–10 G in the average. However, there appears to be a continuous distribution of magnetic field strengths and fluxes, ranging over five decades in flux, from $\Phi = BA \approx 2 \times 10^{17}$ to 10^{23} Mx (Parnell et al. 2009). If we associate the weakest field strengths of $B_{min} \approx 5$ G to the weakest fluxes, we obtain a length scale of $L_{min} \approx \sqrt{\Phi_{min}/B_{min}} \approx 2$ Mm, while the largest sunspots with a field strength of $B_{max} \approx 4000$ G are estimated to have a length scale of $L_{max} \approx \sqrt{\Phi_{max}/B_{max}} \approx 50$ Mm, or 7% of a solar radius (Fig. 4.4 left). The weakest magnetic field structures in the Quiet Sun are called "salt-and-pepper", while the smallest flux concentrations in active regions are referred to as "network" and "magnetic pores" (Fig. 4.4 right). Some studies claim that the Sun's magnetic field is structured over a range of seven orders of magnitude, where four of them are beyond the resolving power of current telescopes (Stenflo 2012). The recycling time of photospheric magnetic fluxes has been measured from 14 hrs (Hagenaar 2001) down to 1.4 hr (Close et al. 2004).

The most remarkable result of the measured magnetic flux structures is the finding of an approximate power law distribution that spans over 5 orders of magnitude (Fig. 4.5; Table 4.1; Parnell et al. 2009),

$$N(\Phi)d\Phi = \Phi^{-1.85\pm0.14}\, d\Phi \quad [\mathrm{Mx}^{-1}\mathrm{cm}^{-2}]\,, \tag{4.2.1}$$

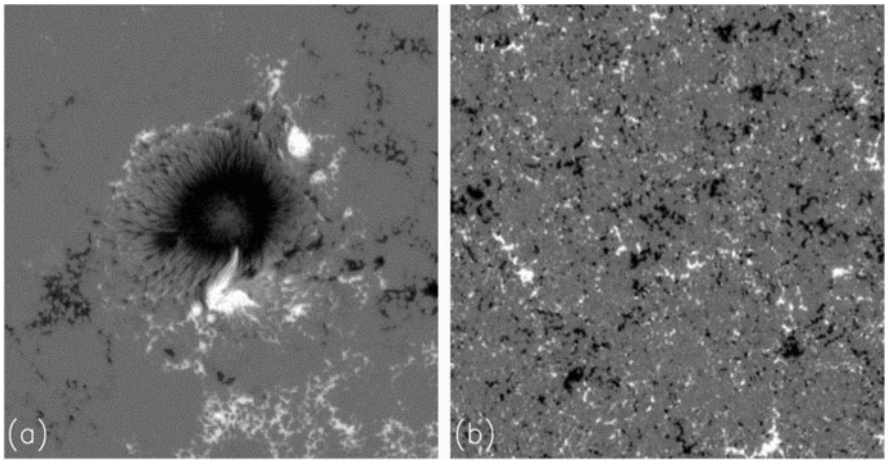

Fig. 4.4 Examples of a large sunspot structure (**a**) and the salt-and-pepper structure in the Quiet Sun (**b**), observed with the *Spectro-Polarimeter (SP)* onboard *SOT/Hinode*, which takes line profiles of the Stokes V parameter in the blue wing of the 6320 Å spectral absorption line, recorded over a slit of 0.15″ (Parnell et al. 2009)

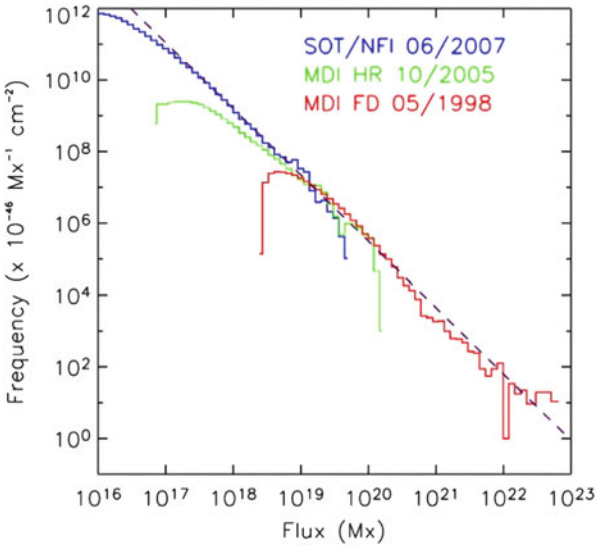

Fig. 4.5 Histogram of magnetic flux features observed with SOT/Hinode and MDI/SOHO. The dashed line represents a power law fit with a slope of $\alpha = -1.85$. Note the range of 5 decades in magnetic flux (Parnell et al. 2009)

This result, however, has been "stitched together" from three different data sets observed with two instruments, i.e., from NFI/SOT/Hinode, and full-disk and high-resolution data from MDI/SOHO. Moreover, the three data sets were observed at different times. A similar value was found also from cellular automaton simulations, i.e., $N(\Phi) \approx \Phi^{-1.5\pm0.05}$ (Fragos et al. 2004).

The question arises, whether this remarkable result can help us to understand the formation process of sunspots and pores in terms of the underlying solar dynamo. Magnetic features observed on the solar surface are believed to be created in the convection zone, either close to the photosphere by a "shallow dynamo", or in the tachocline at the bottom of the convection zone by a "deep dynamo". Schrijver et al. (1997) formulated a set of magneto-chemistry equations and predicted an exponential distribution function for the magnetic fluxes. Parnell (2002) used the same equations, but different assumptions, and predicted a Weibull distribution function. Moreover, simulations show that initially evenly distributed fields form self-organized magnetic structures, such as pores and sunspots (Kitiashvili et al. 2010), which may explain the break in the power law distribution at high magnetic flux values.

If magnetic flux is evenly distributed in the 3-D volume of the convection zone, such as generated by a deep dynamo process, fragmentation would lead to a scale-free size distribution of length scales, $N(L)dL \propto L^{-3}\, dL$, which translates into a size distribution of areas $A = L^2$ as,

$$N^{deep}(A)dA \propto N(L[A])\frac{dL}{dA}dA = A^{-2.0}dA\ . \tag{4.2.2}$$

On the other hand, if the magnetic flux is generated by a shallow dynamo near the surface only, fragmentation would lead to a scale-free size distribution of length scales, $N(L)dL \propto L^{-2}$, which translates into a size distribution of areas $A = L^2$ as,

$$N^{shallow}(A)dA \propto N(L[A])\frac{dL}{dA}dA = A^{-1.5}dA\,. \tag{4.2.3}$$

From cellular automaton simulations, a fractal dimension of $N(L) \propto L^{-1.73\pm0.05}$ was found (Fragos et al. 2004), which is closer to the power law slope value expected for the shallow case, with $N(L) \propto L^{-2}$.

From the the magnetic flux distribution $N(\Phi)$ and area distribution $N(A)$ we can infer a relationship for the scaling between the two parameters Φ and A, which we characterize with a power law exponent β,

$$\Phi \propto A^{\beta}\,. \tag{4.2.4}$$

From the characteristic values of magnetic features listed in Table 2 of Parnell et al. (2009) we find minimum values of $\Phi_{min} = 4.9 \times 10^{18}$ Mx and $A_{min} = 15$ Mm^2, and maximum values of $\Phi_{max} = 128 \times 10^{18}$ Mx and $A_{max} = 2140$ Mm^2 (from MDI data), from which we estimate an approximate power law exponent β of

$$\beta = \frac{\log\left(\Phi_{max}/\Phi_{min}\right)}{\log\left(A_{max}/A_{max}\right)} \approx 0.66\,. \tag{4.2.5}$$

Thus, we obtain the relationship $\Phi(A) \propto A^{0.66}$ from the Parnell et al. (2009) data. Furthermore, we can obtain a prediction of the scaling between the mean magnetic field strength B and the length scale L of each magnetic flux area, using the relationships $\Phi = AB$, $\Phi = A^{\beta}$, and $A = L^2$,

$$B \propto L^{2(\beta-1)} \propto L^{\delta} \propto L^{-0.68}\,, \tag{4.2.6}$$

which approximately agrees with the result of Mandrini et al. (2000), who found a universal scaling law between the mean magnetic field B and the loop length L, derived in the range of $50 \leq L \leq 300$ Mm,

$$B \propto L^{\delta} \approx L^{-0.88\pm0.30}\,, \tag{4.2.7}$$

Note that both data sets predict that the mean magnetic field strength decreases with the length scale of the magnetic area. The fact that the loop length statistics is different in coronal holes, Quiet Sun, and active regions, may complicate the scaling between loop lengths L_{loop} and the sizes L_{mag} of magnetic areas (Wiegelmann and Solanki 2004).

Nevertheless, this simple model based on the results of Parnell et al. (2009) can provide a diagnostic of whether the magnetic features are generated by a deep

Table 4.1 Magnetic flux and area distributions and related scaling laws

	Parnell et al. (2009)	Mandrini et al. (2000)
$N(\Phi) \propto \Phi^{a_\Phi}$	$a_\Phi = -1.85 \pm 0.14$	
$N^{deep}(A) \propto A^{a_A}$	$a_A = -2.0$	
$N^{shallow}(A) \propto A^{a_A}$	$a_A = -1.5$	
$\Phi \propto A^{\beta}$	$\beta = +0.66$	
$B \propto L^{\delta}$	$\delta = -0.68$	$\delta = -0.88 \pm 0.30$

dynamo (if the magnetic area distribution is $N(A) \propto A^{-2.0}$), or by shallow dynamos (if the magnetic area distribution is $N(A) \propto A^{-1.5}$) (see summary of power law slopes in Table 4.1). If both (shallow and deep) dynamos operate, a broken power-law is predicted.

4.3 Bimodal Magnetic Area Distributions

The mathematical form of statistical probability density functions (PDF) of various physical parameters can reveal physical scaling laws and the physical nature of the underlying generation process. For instance, power law (or log-normal) distributions indicate scale-free parameter ranges over which nonlinear energy dissipation processes operate, producing coherently amplified events. In contrast, exponential, Gaussian, or Poissonian distributions indicate random processes that produce incoherent events that are statistically independent. More generalized distribution functions include the Weibull distribution function, which exhibits shapes from a simple power law function to a Rayleigh distribution function (which is Gaussian-like), or the log-normal distribution function, which essentially is close to a Gaussian on a log-scale. The hope is that the mathematical form of a distribution function is generic to a specific physical process, so that it can be used as a diagnostic tool.

Motivated by such statistical arguments, fitting of occurrence frequency distribution functions were carried out for solar magnetic parameters, such as the magnetic flux (Parnell et al. 2009), or sunspot areas, sunspot group areas, and sunspot umbral areas (Meunier 2003; Baumann and Solanki 2005; Zharkov et al. 2005; Zhang et al. 2010; Schad and Penn 2010; Jiang et al. 2011; Nagovitsyn et al. 2012; Tlatov and Pevtsov 2014; Munoz-Jaramillo et al. 2015). Ultimately, the size distribution functions of these magnetic parameters observed in the photosphere are investigated in order to infer information on the size of the solar dynamo, which can have a global scale as large as the depth of the convection zone (the so-called "deep dynamo"), and additionally may consist of small-scale components (the so-called "shallow dynamo").

Tlatov and Pevtsov (2014) investigated the detailed relationship between the magnetic flux $\Phi = AB$, the field strength B, and the sunspot area A, using daily

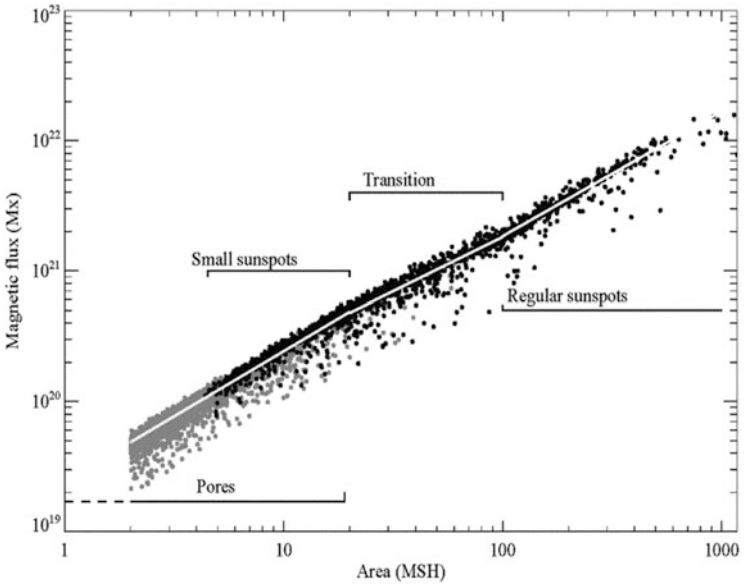

Fig. 4.6 The total magnetic flux $\Phi(A)$ as a function of the area of pores (gray) and sunspots (black). Piecewise linear fits are shown with a white line. The unit of the area is a *millionth solar hemisphere (MSH)* (Tlatov and Pevtsov 2014)

observations from HMI/SDO. The authors fit a function $B_{max} = c_0 + c_1 \log(A)$ to the data and find a bimodal distribution of magnetic fields, which can be expressed by different scaling factors c_0, yielding an average magnetic field strength of $B_{avg} \approx 800$ G for small sunspots and pores ($A \leq 20$ millionth of solar hemisphere, MSH), and of $B_{avg} \approx 600$ G for large sunspots ($A \geq 100$ MSH), with a continuous transition between the two area regimes (Fig. 4.6). The authors attribute this difference to the formation of a regular penumbra in small sunspots. When the sunspot penumbra starts forming, the magnetic field becomes more horizontal, and thus the relation between the vertical field strength and the area of sunspot changes.

Munoz-Jaramillo et al. (2015) study the best-fitting distribution functions for 11 different databases of sunspot areas, sunspot group areas, sunspot umbral areas, and magnetic flux, including the photo-heliographic results of the *Royal Greenwich Observatory (RGO)*, the *Solar Observing Optical Network (SOON)*, the *Pulkovo's catalog of solar activity (PCSA)*, the *Kislovodsk Mountain Astronomical Station (KMAS)*, the HMI/SDO, the *San Fernando Observatory (SFO)*, the *Kitt Peak Vacuum Telescope (KPVT)* bipolar magnetic region and *KPVT/SOLIS* datasets, and the *MDI/SOHO* dataset. An example of a HMI/SDO magnetogram is shown in Fig. 4.7, which illustrates the approximate self-similarity of bipolar magnetic structures over a scale range of about 2 orders of magnitude. A large active region may cover an area with a length scale of almost a half solar radius (Fig. 4.7a), which contains hierarchical subgroups of bipolar structures, as it can be seen when

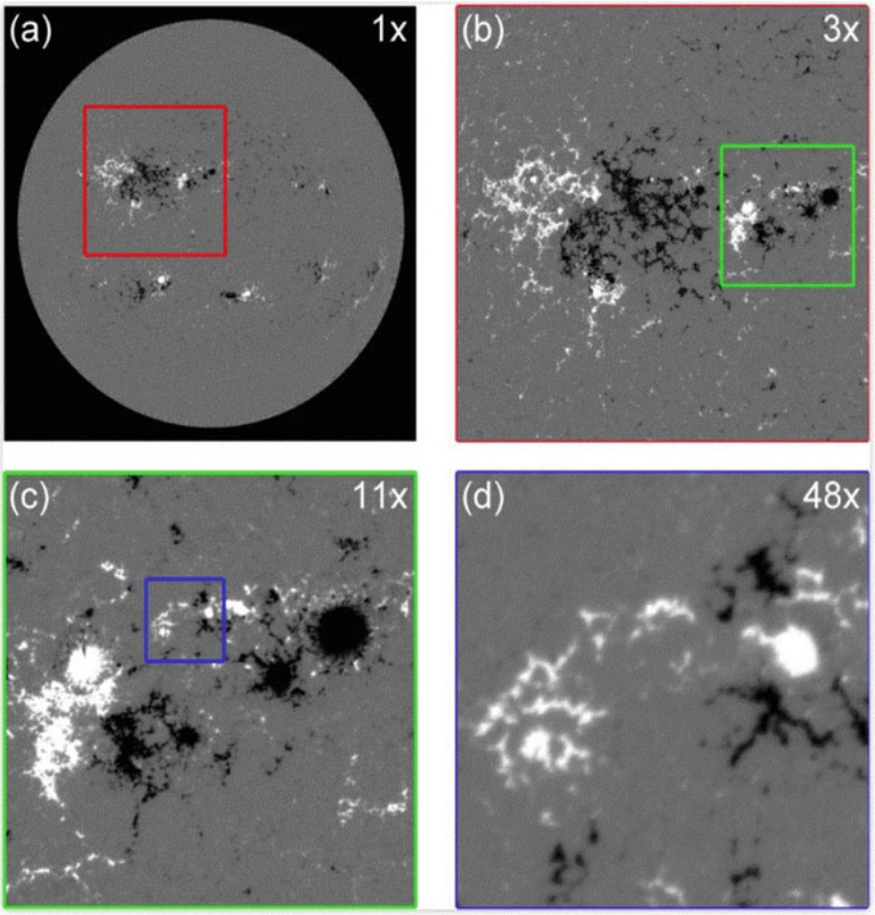

Fig. 4.7 A HMI/SDO magnetogram (2012 June 5) of a large-scale active region is shown (**a**), magnified 3× (**b**), 11× (**c**), and 48× (**d**), which approximately exhibits self-similarity for bipolar structures, spanning over 2 orders of magnitude in length, or 4 orders of magnitude in area (Munoz-Jaramillo et al. 2015)

magnified by a factor of 3 (Fig. 4.7b), a factor of 11 (Fig. 4.7c), or a factor of 48 (Fig. 4.7d). The authors fit log-normal, power law, exponential, and Weibull distribution functions and find that a linear combination of Weibull and log-normal distributions fit the data best, a bimodal function with a separation point around $\approx 10^{21}$–10^{22} Mx in magnetic flux, at $A \approx 10^2$ MSH (Fig. 4.8). The approximate power law shape of the Weibull distribution in the range of 10^{16}–10^{21} Mx found here is compatible with the power law fit of Parnell et al. (2009). The fact that a Weibull distribution was found to be a better fit than a power law function in Munoz-Jaramillo et al. (2015), appears to be a discrepancy to the power-law fits of Parnell et al. (2009), but could possibly be explained with the different detection

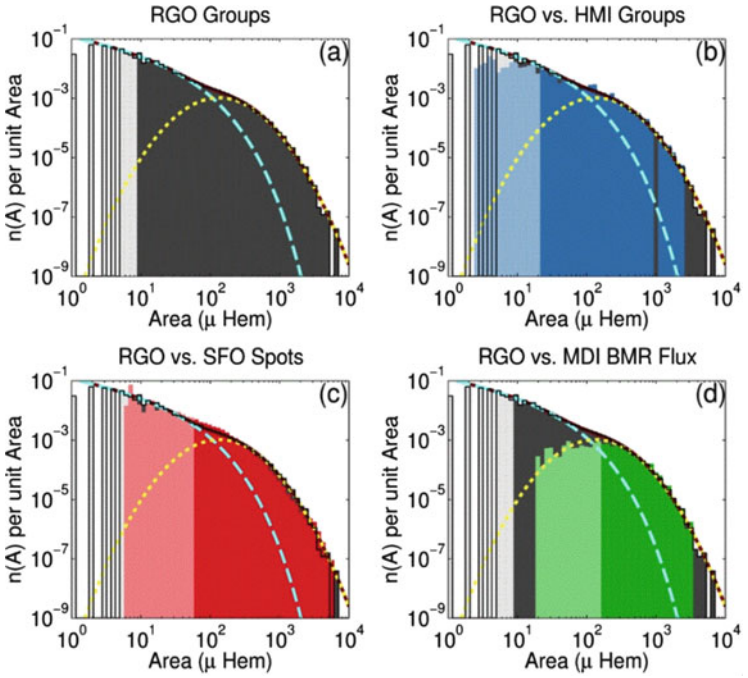

Fig. 4.8 Occurrence frequency size distributions of sunspot areas for 11 different data sets, consisting of a Weibull (dashed blue) and log-normal distributions (dotted yellow line) (Munoz-Jaramillo et al. 2015)

algorithms used in MDI/HR, MDI/FD, and SOT/NFI magnetograms, as well as with the different time durations and solar cycles of the selected data.

Based on the successful fit of bimodal distributions to 11 different datasets with different size ranges, Munoz-Jaramillo et al. (2015) interpret this result as evidence of two separate mechanisms giving rise to visible structures on the photosphere: one directly connected to the global component of the solar dyanmo (and the generation of bipolar active regions), and the other one with the small-scale component of the dynamo (and the fragmentation of magnetic structures due to their interaction with turbulent convection, with a transition between these two types of structures around 10^{21}–10^{22} Mx in flux, or $A \approx 10^2$ MSH). Future MHD simulations of turbulent convection, with flux-emergence and transport throughout the convection zone, may benefit from the additional constraint of these observed magnetic flux distributions and sunspot areas characterized by a bimodal Weibull-lognormal distribution function.

4.4 The Multi-Fractal Photosphere

While the umbra of a photospheric sunspot appears to be space-filling, its surface area A is expected to scale quadratically with its length scale L, i.e., $A \propto L^2$. Outside the umbra, however, a photospheric magnetogram reveals a lot of fragmented magnetic flux, especially in the plages of active regions, down to the ubiquitous salt-and-pepper structure on the entire solar surface. A representative measure of the degree of magnetic flux fragmentation is the fractal (or multi-fractal) dimension, e.g., the 2-D Hausdorff dimension D_2,

$$N(A) \propto A^{D_2} \ , \tag{4.4.1}$$

which defines a size distribution $N(A)$ of areas A with power law index D_2, where the range is limited by $0 < D_2 \leq 2$ for 2-D areas A (in a 2-D Euclidean space). If the fractal dimension is near $D_2 \approx 2$, the sampled structures consist of solid areas, which become curvi-linear near $D_2 \approx 1$, or even dotted near $D_2 \gtrsim 0$. Two widely used methods to infer the fractal dimension are the box-counting method (defined by $D_2 = \log A / \log(L)$), and the perimeter-area method (defined by $P \approx A^{D_2/2}$, with P being the perimeter length).

A compilation of fractal dimensions measured in photospheric magnetograms is given in Table 4.2. The solar granulation has a typical spatial scale of $L = 1000$ km, or a perimeter of $P = \pi L \approx 3000$ km. Roudier and Muller (1986) measured the areas A and perimeters P of 315 granules and found a power law relation $P \propto A^{D/2}$, with $D = 1.25$ for small granules (with perimeters of $P \approx 500$–4500 km) and $D = 2.15$ for large granules (with $P = 4500$–$15,000$ km). The smaller granules were interpreted in terms of turbulent origin, because the predicted fractal dimension of an isobaric atmosphere with isotropic and homogeneous turbulence is $D = 4/3 \approx 1.33$ (Mandelbrot 1977). Similar values were found by Hirzberger et al. (1997). Bovelet and Wiehr (2001) tested different pattern recognition algorithms (Fourier-based recognition technique FBR and multiple-level tracking MLT) and found that the value of the fractal dimension strongly depends on the measurement method. The MLT method yielded a fractal dimension of $D \approx 1.1$, independent of the spatial resolution, the heliocentric angle, and the definition in terms of temperature or velocity. Meunier (1999) evaluated the fractal dimension with the perimeter-area method and found $D = 1.48$ for supergranular structures to $D = 1.68$ for the largest structures, while the linear size-area method yielded $D = 1.78$ and $D = 1.94$, respectively. In addition, a solar cycle dependence was found by Meunier (2004), with the fractal dimension varying from $D = 1.09 \pm 0.11$ (minimum) to $D = 1.73 \pm 0.01$ for weak-field regions ($B_m < 900$ G), and $D = 1.53 \pm 0.06$ (minimum) to $D = 1.80 \pm 0.01$ for strong-field regions ($B_m > 900$ G), respectively. A fractal dimension of $D = 1.41 \pm 0.05$ was found by Janssen et al. (2003), but the value varies as a function of the center-to-limb angle and is different for a speckle-reconstructed image that eliminates seeing and noise.

Table 4.2 Area fractal dimension D_2 of scaling between length scale L and fractal area $A(L) \propto L^{D_2}$ of various solar phenomena observed in white light and in magnetograms

Wavelengths regime and phenomenon (reference in superscript)	Method	Area fractal dimension D
White-light of granules[a]	Perimeter area	1.25, 2.15
White-light of granules[b]	Perimeter area	1.3, 2.1
White-light of granular cells[b]	Perimeter area	1.16
White-light of granules[c]	Perimeter area	1.09
Magnetogram super-granulation[d]	Perimeter area	1.25
Magnetograms of small scales[e]	Perimeter area	1.41 ± 0.05
Magnetograms of active regions[f,g]	Linear size area	1.56 ± 0.08
Magnetograms of plages[h]	Linear size area	1.54 ± 0.05
Magnetograms of active regions[i]	Linear size area	1.78–1.94
	Perimeter area	1.48–1.68
Magnetograms of active regions[j]	Perimeter area	
– Total		1.71–1.89
– Cycle minimum		1.09–1.53
– Cycle rise		1.64–1.97
– Cycle maximum		1.73–1.80
Magnetograms Quiet Sun, active regions[k]	Box-counting	Multifractal
Magnetograms of active regions[l,m]	Box-counting	Multifractal
Magnetograms of active regions[n]	Box-counting	1.25–1.45

References: [a]Roudier and Muller (1986); [b]Hirzberger et al. (1997); [c]Bovelet and Wiehr (2001); [d]Paniveni et al. (2005); [e]Janssen et al. (2003); [f]Lawrence (1991); [g]Lawrence and Schrijver (1993); [h]Balke et al. (1993); [i]Meunier (1999); [j]Meunier (2004); [k]Lawrence et al. (1993); [l]Cadavid et al. (1994); [m]Lawrence et al. (1996); [n]McAteer et al. (2005)

A completely different approach to measure the fractal dimension D was pursued in terms of a 2-D diffusion process, finding fractal diffusion with dimensions in the range of $D \approx 1.3$–1.8 (Lawrence 1991) or $D = 1.56 \pm 0.08$ (Lawrence and Schrijver 1993) by measuring the dependence of the mean square displacement of magnetic elements as a function of time. Similar results were found by Balke et al. (1993). The results exclude Euclidean 2-D diffusion but are consistent with percolation theory for diffusion of clusters at a density below the percolation threshold (Lawrence and Schrijver 1993; Balke et al. 1993).

Fractal dimensions were also evaluated with a box-counting method, finding a range of $D \approx 1.30$–1.70 for chromospheric network structures in a temperature range of $T = 10^{4.5} - 10^6$ K (Gallagher et al. 1998), a value of $D \approx 1.4$ for so-called *Ellerman bombs* (Georgoulis et al. 2002), which are short-lived brightenings seen in the wings of the Hα line from the low chromosphere, or a range of $D \approx 1.25$–1.45 from a large survey of 9342 active region magnetograms (McAteer et al. 2005). In the most recent work it was found that the concept of mono-fractals has to be generalized to multi-fractals (Fig. 4.9) to quantify the spatial structure of solar magnetograms more accurately (Lawrence et al. 1993, 1996; Cadavid et al. 1994; McAteer et al. 2005; Conlon et al. 2008).

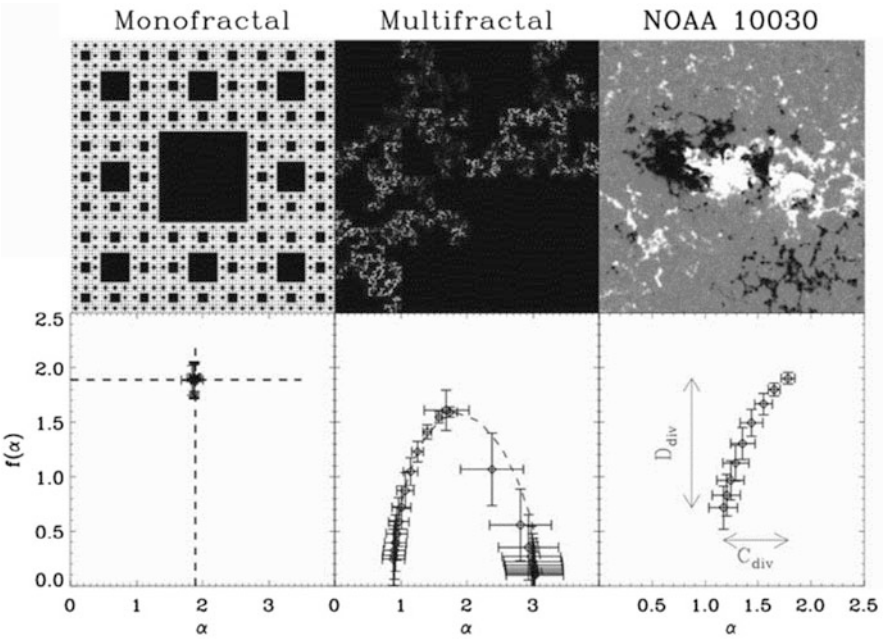

Fig. 4.9 *Top:* A monofractal image, a multi-fractal image, and a magnetogram of an active region. *Bottom:* Multi-fractal spectra with a spectrum of exponents $f(\alpha)$, each with relative strength or significance α (Conlon et al. 2008)

The physical understanding of solar (or stellar) granulation has been advanced by numerical magneto-convection models and N-body dynamic simulations, which predict the evolution of small-scale (granules) into large-scale features (meso or supergranulation), organized by surface flows that sweep up small-scale structures and form clusters of recurrent and stable granular features (Hathaway et al. 2000; Berrilli et al. 2005; Rieutord et al. 2008, 2010). The fractal structure of the solar granulation is obviously a self-organizing pattern that is created by a combination of subphotospheric magneto-convection and surface flows, which are turbulence-type phenomena.

The generation of magnetic structures that bubble up from the solar convection zone to the solar surface by buoyancy, observed as emerging flux phenomena in form of active regions, sunspots, and pores, can be statistically described as random, self-organization (SO), self-organized criticality (SOC), percolation, or diffusion process. Random processes produce incoherent structures, in contrast to the coherent magnetic flux concentrations observed in sunspots. A self-organization (SO) process needs a driving force and a counter-acting feedback mechanism that produces ordered structures (such as the convective granulation cells). A SOC process exhibits power law size distributions of avalanche sizes and durations. The finding of a fractal dimension in magnetic features alone is not a sufficient condition

to prove or rule out any of these processes. Nevertheless, it yields a scaling law between areas ($A \propto L^{D_2}$) or volumes ($V \propto L^{D_3}$) and length scales L that quantifies scale-free (fractal) processes in form of power laws and can straightforwardly be incorporated in SOC-like models.

4.5 Mini-Granulation

The solar photosphere exhibits a pattern of "bubbling" cells (like boiling water in a frying pan), which is called "photospheric granulation" and has been interpreted in terms of hydrodynamic convection cells (Fig. 4.10). The central part of a granulation cell is occupied with upflowing plasma, which then cools down and descends in the surrounding edges, which consequently appear to be darker than the center, because a cooler temperature corresponds to darker white-light emission. The photospheric temperature is $T_s = 5780$ K, the typical size of a granule is $w \approx 1500$ km, and the life time is about 8–20 min.

The underlying physical mechanism of convection has been studied in great detail in terms of the Rayleigh-Bénard instability, known as the Lorenz model (Lorenz 1963), described also in the monographs of Chandrasekhar (1961) and Schuster (1988). The basic ingredients of the (hydrodynamic) Lorenz model are the Navier-Stokes equation, the equation for heat conduction, and the continuity equation. The Lorenz model can describe the transition from heat conduction to convection rolls, where Lorenz discovered the transition from deterministic to chaotic system dynamics. Thus, the Lorenz model demonstrates that a temperature gradient (for instance below the photosphere) transforms (a possibly turbulent) random motion into a highly-organized rolling motion (due to the Rayleigh-Bénard instability) and this way organizes the plasma into nearly equi-sized convection rolls that have a specific size (such as $w \approx 1500$ km for solar granules). A self-organization process thus creates order (of granules with a specific size) out of randomness (of the initial turbulent spectrum). Since convection is the main energy transport process inside the Sun down to $0.7 R_\odot$, larger convection rolls than the granulation pattern can be expected. Krishan (1991) argues that the Kolmogorov turbulence spectrum $N(k) \propto k^{-5/3}$ extends to larger scales and possibly can explain the observed hierarchy of structures (granules, mesogranules, supergranules, and giant cells) by the same self-organization process (for a review of self-organization processes in astrophysics see Aschwanden et al. 2018).

At smaller scales, a subpopulation of mini-granular structures has been discovered recently, in the range of $w \approx 100$–600 km, predominantly confined to the wide dark lanes between regular granules, often forming chains and clusters, but being different from magnetic bright points (Abramenko et al. 2012). A set of TiO images of solar granulation acquired with the 1.6 meter *New Solar Telescope (NST)* at *Big Bear Solar Observatory (BBSO)* was utilized. The high-contrast speckle-reconstructed images of Quiet-sun granulation (Fig. 4.10), allowed to detect, besides the regular-size granules, the small granular-like features in dark inter-granular

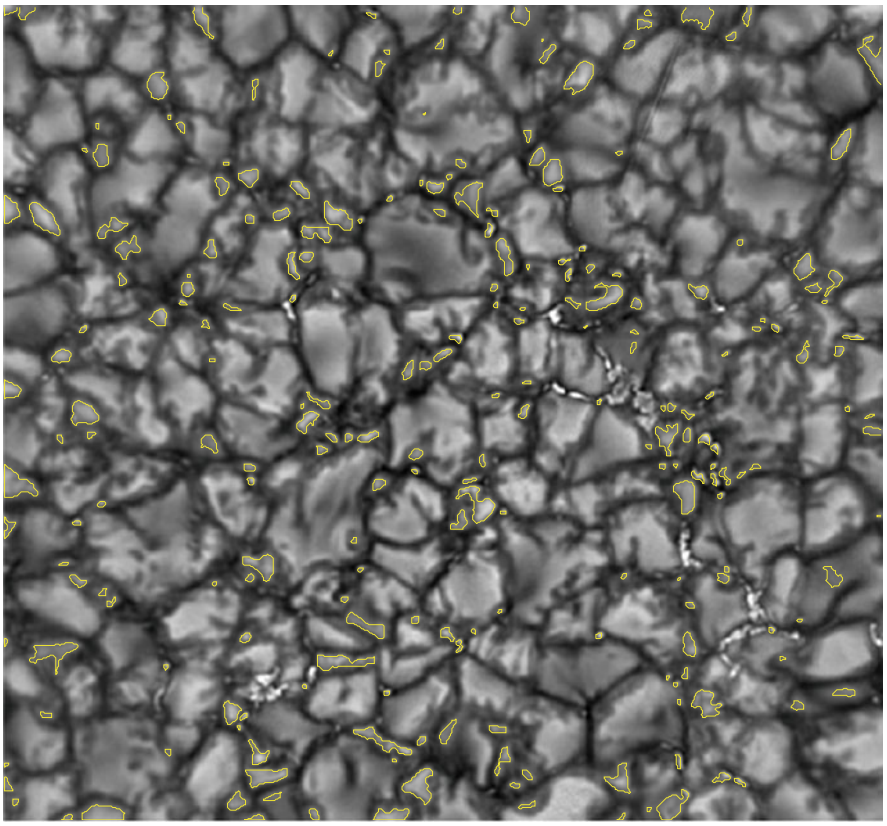

Fig. 4.10 A TiO image of the solar surface is shown, containing normal granules and mini-granules in a Quiet Sun region, observed with the *New Solar Telescope (NST)*. Mini-granules are outlined with yellow contours, which show granular-like features of sizes below 600 km located in dark intergranular lanes. Note that the mini-granules do not coincide with magnetic bright points (Abramenko et al. 2012)

lanes, named as *mini-granules*. Mini-granules are very mobile and short-lived. They are predominantly located in places of enhanced turbulence and close to strong magnetic fields in inter-granular lanes. The equivalent size of detected granules was estimated from the circular diameter of the granule area. The resulting *probability density functions (PDF)* for 36 independent snapshots are shown in gray in the left frame of Fig. 4.11). The average PDF (the red histogram) changes its slope in the scale range of $\approx$ 600–1300 km. This varying power law PDF is suggestive that the observed ensemble of granules may consist of two populations with distinct properties: regular granules and mini-granules. A decomposition of the observed PDF showed that the best fit is achieved with a combination of a power law function (for mini-granules) and a Gaussian function (for granules). Their sum fits the observational data (Fig. 4.11). Mini-granules do not display any characteristic

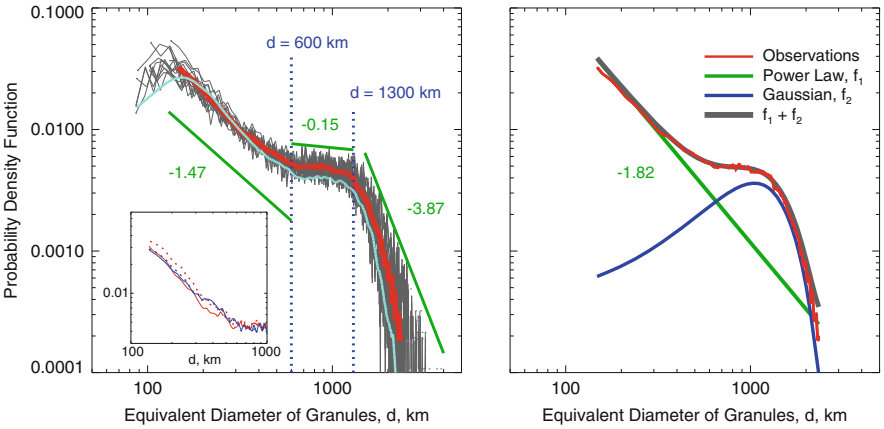

Fig. 4.11 The probability density function of the equivalent diameter of granules (in units of km) is shown, observed in Quiet Sun regions with the *New Solar Telescope (NST)*. The regular granules have a size of $w \approx 500$–2000 km, while the range of $w \approx 100$–500 km exhibits the new phenomenon of "mini-granules" (Abramenko et al. 2012)

("dominant") scale. This non-Gaussian distribution of sizes implies that a more sophisticated mechanism with more degrees of freedom may be at work, where any small fluctuation in density, pressure, velocity and magnetic field may have significant impact and affects the resulting dynamics. It is worth to note that a recent direct numerical simulation attempt (Van Kooten and Cranmer 2017) produced the PDF of granular size (Fig. 4.12) in agreement with the observed one in Fig. 4.11. The authors concluded that the population of mini-granules is intrinsically related to non-linear turbulent phenomena, whereas Gaussian-distributed regular granules originate from near-surface convection.

The size distribution of granulation cells in the solar photosphere does not form a power law distribution, but clearly shows a preferred spatial scale of $\approx$ 1500 km, which renders a regular spatial pattern, rather than a scale-free distribution. However, a power law distribution has been found for the newly discovered "mini-granules" in a size range of 100–600 km, which is not consistent with a self-organizing convective process that creates bubbles of equal sizes. The physical process of convection that is driven by a temperature gradient and the Rayleigh-Bénard instability is well-understood and known as the Lorenz model. A caveat is how much the magnetic field plays a role in the solar convection zone, requiring a model with magneto-convection and hydromagnetic (Parker and Kruskal-Schwarzschild) instabilities. In summary, two different physical mechanisms are required to explain the two different types of distribution functions for "regular granules" and "mini-granules": The Gaussian size distribution of regular granules is consistent with the self-organizing convection process, while the power law size distribution of "mini-granules" could be related to nonlinear turbulence (as simulated by Van Kooten and Cranmer 2017).

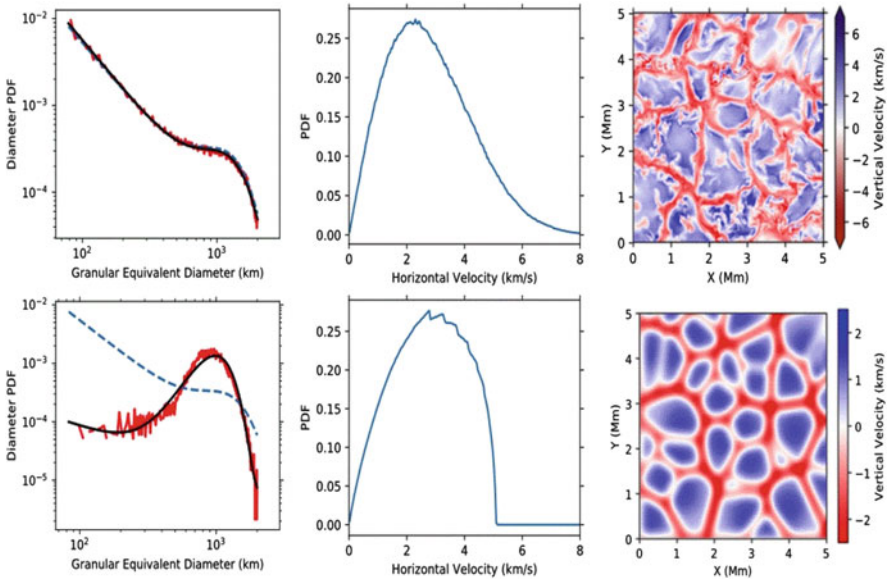

Fig. 4.12 Comparison of MURaM (top) and ROUGH (bottom) numerical MHD simulations of solar granulation, showing the probability distribution functions (PDF) of the granule sizes (left panels, red), and the fitted distributions of Abramenko et al. (2012), renomarlized to this plotting range and fitted to the simulated data (left panels, black), and the histogram of horizontal velocity magnitudes at all pixels in the simulation (middle panels), and velocity maps (right panels) (Van Kooten and Cranmer 2017)

4.6 Quiet-Sun and Polar Fields

Solar magnetism occurs on all scales, as mean field (poloidal and toroidal) components that cover the entire hemisphere, as well as on progressively smaller scales as active regions, sunspots, and magnetic pores, up to the diffraction limit of the largest telescopes (de Wijn et al. 2009; Lagg et al. 2017), or beyond (Stenflo 2012). Granular flows in the photosphere sweep flux into intergranular lanes, where it clumps into small concentrations of mostly vertical field with strengths in excess of 1000 G, coinciding with bright points and faculae in white light, best visible in plages of active regions.

In the Quiet Sun, supergranular flows are concentrated in the magnetic network that outline supergranular cells in intermittent patterns. The internetwork magnetic field in the Quiet Sun has been found to carry strong horizontal fields ubiquitously (Lites et al. 2008), which requires very sensitive magnetometers for their detection, such as SOT/SP onboard Hinode. These small-scale magnetic fields in the Quiet Sun have been called "granular fields" (Lin and Rimmele 1999), "horizontal Quiet-Sun fields" (Lites et al. 1996), or "seething fields" (Harvey et al. 2007). Internetwork fields have traditionally been measured with the Zeeman effect, while

the turbulent field has been probed mainly with the Hanle effect, which reveals small-scale "hidden" magnetic flux (Stenflo 2004). The weakest fluxes measured in internetwork features with present instrumentation has a magnetic flux of $\approx 10^{16}$ Mx (Fig. 4.5). The rate of magnetic flux in internetwork fields is found to be $\approx 10^2$ times larger than in ephemeral active regions, and about a factor of $\approx 10^4$ larger than in active regions, but the decay time scale is reciprocally shorter, so that it is not clear what component dominates the net flux emergence. Before the Hinode mission, typical average field strengths of $\approx$ 2–5 G were measured in Quiet Sun regions, while average field strengths of $\approx$ 20 G were measured in the internetwork with sub-arcsecond ($0.5''$) spatial resolution (Dominquez Cerdena et al. 2003), and $\approx$ 11 G with the Hinode Spectro-Polarimeter ($0.32''$) (Lites et al. 2008).

In the solar polar regions, where the global magnetic field is open and where the fast solar wind originates, magnetic field measurements are very challenging due to the variable seeing, combined with a strong intensity gradient and the foreshortening effect at the solar limb. A breakthrough took place with the Hinode/SOT instrument, which has a diffraction-limited spatial resolution of $0.2''$–$0.3''$. This instrument revealed many vertically oriented magnetic flux tubes with field strengths as strong as $\approx$ 1000 G within a latitude range of 70° and 90° (Tsuneta et al. 2008). Hinode observed the solar polar region on 2007 March 16 when the south pole was located 7° inside the visible solar disk. All 4 Stokes profiles were measured in two Fe I lines (6301.2 and 6301.5 Å) and the magnetic field strength B was inverted by fitting a Milne-Eddington atmosphere to the Stokes profiles. A view of the reconstructed magnetogram from the direction of the south pole is shown in Fig. 4.13, which exhibits isolated unipolar patches, some with field strengths reaching over 1000 G, while all have the same polarity, consistent with the global polarity of the south polar region. The polar coronal hole extends from 90° down to 60°–70° in latitude, and thus the entire polar region mapped in Fig. 4.13 represents the photospheric base of the polar coronal hole.

The magnetic landscape of the polar region is characterized by vertical kilogauss patches with super-equipartition field strength, a coherent polarity in each hemisphere, and ubiquitous weaker transient horizontal magnetic fields. Histograms of magnetic field strengths, intensities, and filling factors are shown in Fig. 4.14. The lifetime of the magnetic concentrations in the Quiet Sun has been estimated from MDI/SOHO data to be $\approx$ 1 hr for 2.5×10^{18} Mx fluxes, and $\approx$ 10 hrs for 10×10^{18} Mx fluxes. The total magnetic flux of this area is estimated to be $\Phi = 2 \times 10^{22}$ Mx, while the area covers $A = 2.1 \times 10^{18}$ cm^{-2} (Tsuneta et al. 2008). Combining the footpoint areas of all flux tubes with $B > 200$ G, an expansion factor of ≈ 345 is required to fill the entire space of the coronal hole, (for modeling of vertically expanding magnetic structures see examples in Fig. 4.15). If the polar field with the same total magnetic flux $\Phi \approx BfS$ were uniformly distributed (S being the total magnetic area and f being the filling factor), the estimated effective field strength would be about 10 G, as measured with SOT/SP in Quiet Sun regions. Thus the surface poloidal magnetic energy is approximately 90 times larger than in the case of a uniform magnetic field, if we take $B \approx 900$ G, corresponding to the peak of the energy probability density function shown in Fig. 4.14b. The equi-partition

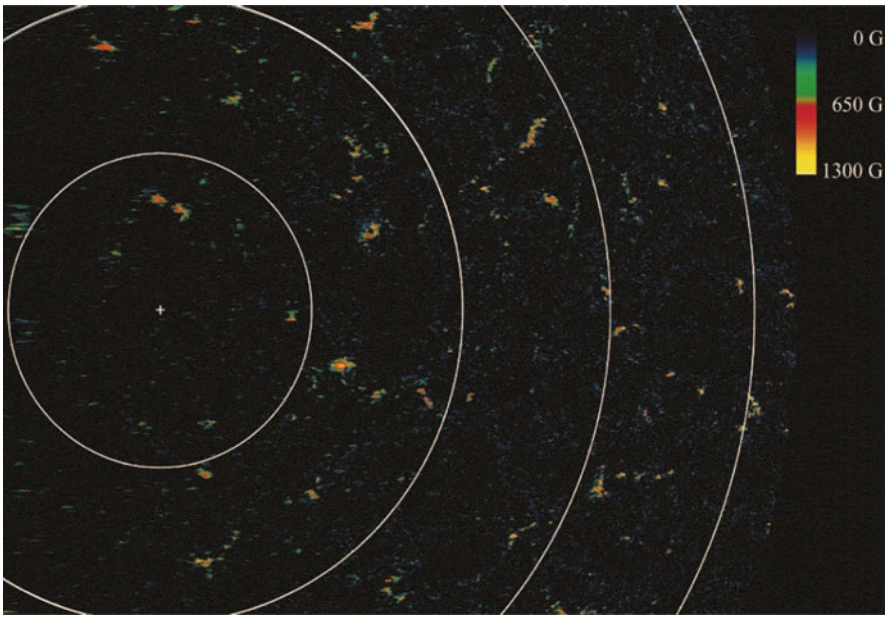

Fig. 4.13 South polar view of the magnetic field strength observed on 2007 March 16. The magnetic field strength (color-coded in the range of $B = 0$–1300 G) is rendered for pixels above a noise threshold (Tsuneta et al. 2008)

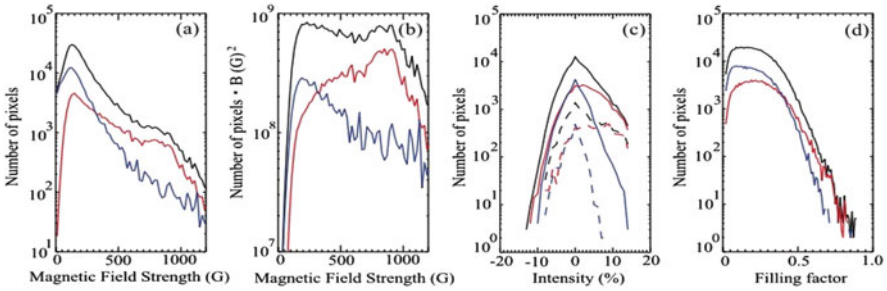

Fig. 4.14 Statistics of pixels as a function of the magnetic field strength (**a**,**b**), intensity (**c**), and filling factors (**d**). Red histograms indicate the vertical field, blue the horizontal field, and black the total field. The histogram is multiplied with the function B^2 in (**b**). Histograms of continuum intensity for magnetic field strengths of 300 B (solid lines) and 800 G (dashed lines) are shown in (**c**). All panels are for latitudes above 75° (Tsuneta et al. 2008)

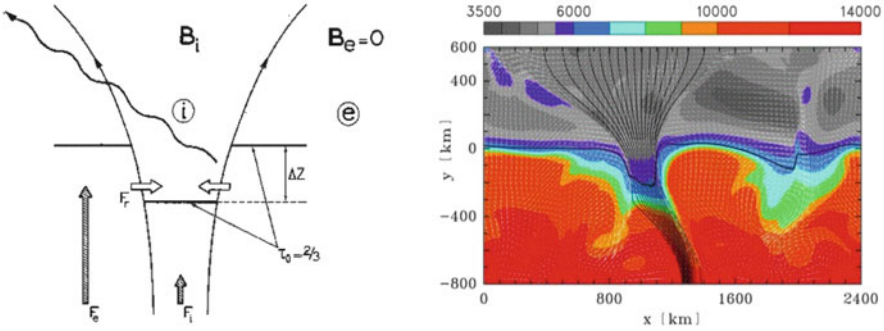

Fig. 4.15 Examples of modeling magnetic elements with vertically expanding fields: *Left:* Analytic magneto-static flux tube model. *Right:* a 2-D MHD model of a flux sheet (de Wijn et al. 2009)

field strength B_e, at which the magnetic energy is equal to the kinetic energy of the surface granular motion, is $B_e = (4\pi\rho v^2)^{1/2}$. The typical value of B_e is ≈ 400 G for granules, with a velocity of $v = 2 \times 10^5$ cm s^{-1}, indicating that the magnetic field strength for the majority of the patches is larger than the equi-partition field strength.

Tsuneta et al. (2008) interpret the findings as follows: The observed unipolar flux tubes scattered about the polar region are considered to represent poloidal seed for toroidal fields (Wang et al. 1989). Magnetic flux is transported to the polar regions by meridional flows and supergranular diffusion in the flux-transport dynamo model (Dikpati and Charbonneau 1999). Since the magnetic field takes the form of such isolated flux tubes with super-equipartition strength, instead of the diffuse weak mean field assumed in the flux-transport dynamo, flux transport on the Sun occurs by means of an aerodynamic (drag) force against the magnetic tension force and may be more complicated than in the mean field case assumed in the models (Tsuneta et al. 2008).

4.7 Penumbral Dynamics

The structure of a sunspot is determined by the local interaction of magnetic fields and by the magneto-convection near the solar surface (for recent reviews see: Solanki 2003; Thomas and Weiss 2004, 2008; Borrero and Ichimoto 2011; Rempel and Schlichenmaier 2011). The dark central umbra is surrounded by a filamentary penumbra, whose complicated fine structure has only recently been revealed by high-resolution observations. The magnetic field in the penumbra has an intricate interlocking-comb structure (Fig. 4.16), where some field lines with associated outflows of gas dive back down below the solar surface at the outer edge of the spot (Thomas et al. 2002). They stay submerged, although one would

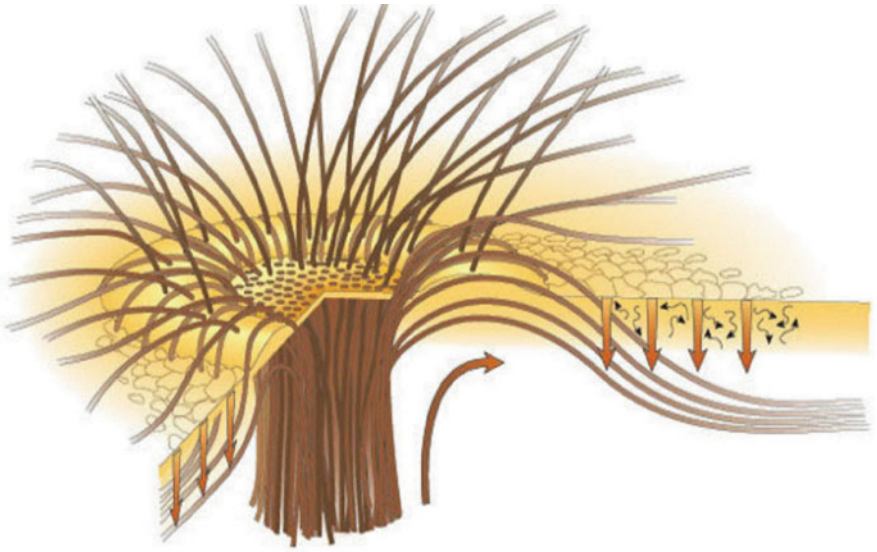

Fig. 4.16 Sketch showing the interlocking-comb structure of the magnetic field in the filamentary penumbra of a sunspot. The bright radial filaments, where the magnetic field is inclined (at about 40° to the horizontal in the outer penumbra), alternate with dark filaments in which the field is nearly horizontal. Within the dark filaments, some magnetic flux tubes (bundles of magnetic field) extend radially outward beyond the penumbra along an elevated magnetic canopy, while other returning flux tubes dive back below the surface. The sunspot is surrounded by a layer of small-scale granular convection (thin quiggly black arrow) embedded in the radial outflow (thick curved brown arrow) associated with a long-lived annular supergranule (the moat cell). The submerged parts of the returning flux tubes are held down by turbulent pumping (indicated by thick vertical brown arrow) due to granular convection in the moat. There is also a persistent horizontal outflow in the penumbra (the Evershed flow), which is mostly confined to thin, nearly horizontal, radial channels with the dark filaments (Thomas et al. 2002)

expect that magnetic buoyancy will bring them quickly back to the surface. Thomas et al. (2002) demonstrated that the field lines are kept submerged outside the spot by turbulent, compressible convection, which is dominated by strong coherent descending plumes. Moreover, this downward pumping of magnetic flux explains the origin of the interlocking-comb structure of the penumbral magnetic field, and the behaviour of other magnetic features near the sunspot.

While the penumbral model of Thomas et al. (2002) proposed a downward pumping mechanism with an interlocking comb structure (Fig. 4.16), alternative models were created with uncombed magnetic fields (Fig. 4.17), such as the *"embedded flux tube model"* (Solanki and Montavon 1993), or the *"field-free gap model"* (Spruit and Scharmer 2006; Scharmer et al. 2011). While each of these empirical models could explain a subset of observables, none of them could match all of them, such as the origin of the Evershed flow, the heat flux of the penumbral surface, the overturning convective motion, the inward migration of penumbral grains, or the asymmetric Stokes profiles observed in the penumbra.

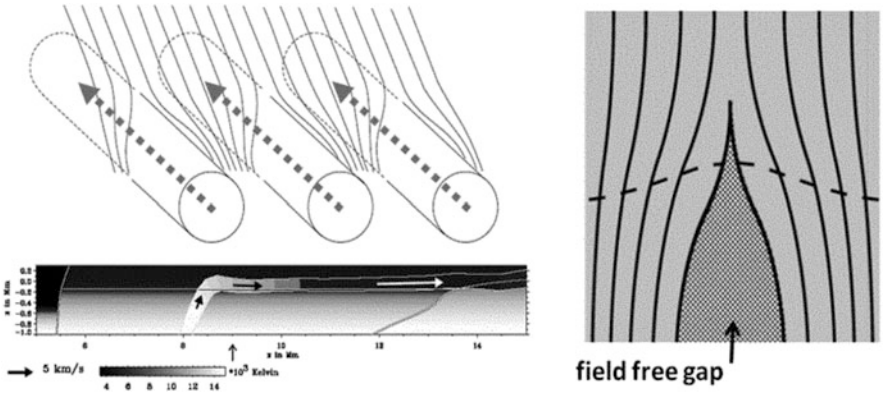

Fig. 4.17 Models for explaining the uncombed penumbral structure: the embedded flux tube model (top left; Solanki and Montavon 1993); the rising flux-tube model (bottom left: Schlichenmaier et al. 1998); the field-free gap model (right: Spruit and Scharmer 2006)

Recent Ca II 8542 Å data are found to be consistent with an inverse Evershed flow, where a critical (sonic) or supersonic siphon flow along super-penumbral flux tubes accelerates plasma that abruptly attains subcritical velocity through a standing shock in or near the penumbra (Choudhary and Beck 2018).

Ultimately, progress in sunspot modeling occurred once the transition from simplified empirical (analytical) models to radiative 3-D MHD simulations was achieved, which triggered a dramatic change in sunspot models (Rempel and Schlichenmaier 2011). Previous empirical models were formulated with magnetostatic MHD models, with parameterized energy transport, with predefined geometries (e.g., flux tubes, field-free gaps, convective rolls), which prevented a self-consistent explanation of all aspects of penumbral structure (energy transport, filamentation, Evershed flow). In recent 3-D radiative MHD simulations, overturning convection is the key element to understand energy transport, filamentation leading to fine structure, and the driving of strong outflows. In the big picture, these 3-D MHD simulations should also be able to explain the subsurface structure of sunspots as well as the sunspot formation.

Due to the formidable numerical challenges, recent 3-D radiative MHD simulations started first with the smallest structures of umbral dots, continued then to piece-wise sections of penumbrae, and finally reached full sunspots. Rempel et al. (2009) performed a simulation of an opposite polarity sunspot pair in a domain of $98 \times 49 \times 6$ Mm at a resolution of 32 km in the horizontal direction and 16 km in the vertical, requiring a total of 1.8×10^9 grid points (Fig. 4.18). This simulation presents for the first time an extended outer penumbra with a strong radial outflow that has a filling factor close to unity and average velocities of up of 5 km s^{-1} (and peak flow speed of 14 km s^{-1}). The location of regions with radial outflows is strongly related to the average inclination angle ($\gtrsim 45°$) of the magnetic field.

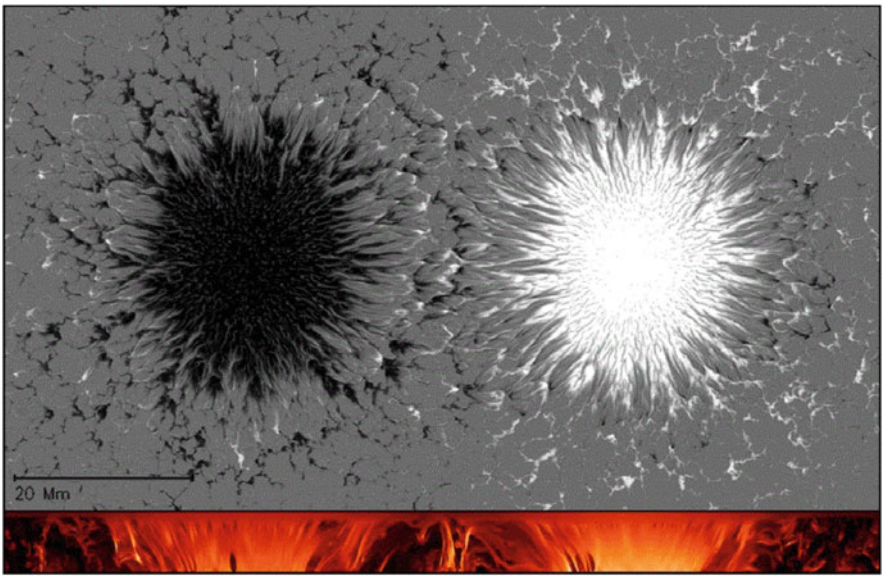

Fig. 4.18 Still image of a time-dependent 3-D radiative MHD simulation of an opposite polarity sunspot pair. The tope panel shows a magnetogram of the vertical field, with magnetic field values ranging from −3000 to +3000 G. The bottom panel depicts the magnetic field from a vertical cut through the center of both sunspots, with a range of 0 to 10,000 G (Rempel et al. 2009)

A unified picture of numerical simulations of the penumbra is discussed in Borrero and Ichimoto (2011). The *embedded flux-tube model*, or the *rising hot flux tube* with the dynamic evolution of the flux tube explains a number of observational aspects about the fine scale features of the penumbra, such as the origin of the Evershed flow, inward migration of penumbral grains, and asymmetric Stokes profiles observed in the penumbra, but faces difficulties when attempting to explain the heat transport to the penumbral surface. In the *field-free gap penumbral model*, the gap is formed by a convecting hot and field-free gas protruding upward into the background (oblique) magnetic fields of the penumbra, and is supposed to be the region that harbors the Evershed flow. It has an advantage in explaining the heat transport to the penumbral surface and twisting appearance of penumbral bright filaments, but does not address the origin of the Evershed flow. Thus, both the embedded flux-tube model and the field-free gap model have their own advantages but also considerable shortcomings. The recent 3-D radiative MHD simulations are able to reproduce the radial filamentary structure of the penumbra as seen in continuum images, the uncombed structure of the magnetic field, Evershed outflows along the filaments with a nearly horizontal magnetic field, and overturning convective motions in upwelling plumes. According to Rempel (2011), the Evershed flow is driven by vertical pressure forces in upflows that are deflected into the horizontal direction through the Lorentz-force generated by the horizontally stretched magnetic fields in flow channels, and the radial flow velocity reaches up to

8 km s^{-1} at the depth of $\tau_c = 1$ with a rapid decline toward the higher atmospheric layers. Thus, the recent 3-D radiative MHD simulations have begun to reproduce many details of fine scale dynamics and structure of the magnetic field observed in the penumbra.

4.8 Rotating Sunspots

The rotation of sunspots, first detected over a century ago (Evershed 1910), has at least two possible interpretations: either (1) a helically twisted vertical magnetic field structure is pushed upward through the photosphere, or (2) a vertically balanced structure is rotated by forces that act in the azimuthal direction of a rotationally symmetric sunspot. Either way, this dynamic phenomenon can reveal important information on the solar dynamo and its generation of magnetic fields inside the Sun. For examples of twisted sunspots, sigmoids, and quadrupoles see Fig. 4.19.

Observations of sunspot rotation in the new millennium were furnished in white-light from TRACE and in soft X-rays from *SXT/Yohkoh* data (Brown et al. 2003), exhibiting rotation angles about their umbral center up to 200° over a period of 3–5 days. From seven cases of identified rotating sunspots, two were found to be associated with sigmoid structures in soft X-rays, and six events associated with GOES C- to X-class flares. Using the *non-linear affine velocity estimator (NAVE)* method (Min and Chae 2009; Zhu et al. 2012; Wang et al. 2014), rotation angles up to 540° were measured (Min and Chae 2009). Among 82 sunspots with strong flux emergence, 63 showed rotational angular velocities larger than 0.4° hr^{-1} (Zhu et al. 2012). Using the travel-time delay method in local helioseismology, strong shear flows beneath a rapidly rotating sunspot was detected (Kosovichev 2002; Zhao and Kosovichev 2003). Sub-photospheric flows associated with sunspot rotations were also detected with the ring-diagram technique (Jain et al. 2012). From statistics of 103 years of sunspot data it was found that young groups rotate faster than old spot groups (Hiremath 2002; Ruzdjak et al. 2004), and that the observed rotation rates approximately match the rotation speed inferred from helioseismology (Hiremath 2002). Statistics of 182 rotating sunspots was gathered from MDI/SOHO, TRACE, an Hinode data, exhibiting a similar ratio of clockwise to counterclockwise rotations in both hemispheres (Yan et al. 2008).

The relationship between rotating sunspots and the triggering of a flare accompanied by a sigmoid eruption, most likely driven by a kink instability, is overwhelming. Evidence is given, e.g., for the case of the largest proton event (2001 November 4) in cycle 23 (Tian and Alexander 2006), the 2006 December 13 flare and CME event (Zhang et al. 2017), the 2003 August 5 flare (Yan and Qu 2007), flares in the super active region NOAA 10486 (Zhang et al. 2008), the X17 eruptive flare on 2003 October 28 (Kazachenko et al. 2010), the X2.2-class flare on 2011 February 15 in NOAA 11158 (Jiang et al. 2012; Vemareddy et al. 2012; Wang et al. 2014; Li and Liu 2015), the flare and CME events on 2000 February 9–10 in NOAA 08858

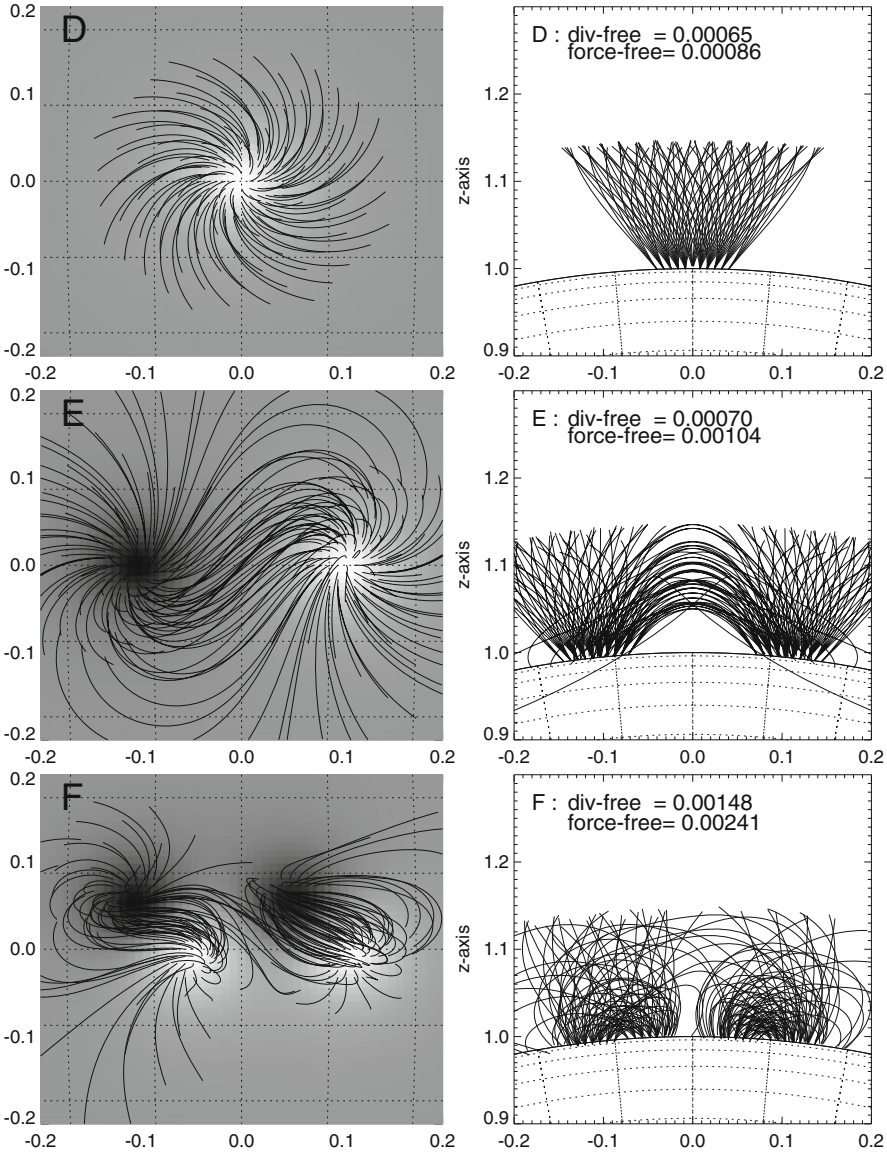

Fig. 4.19 The magnetic field of a rotated sunspot (top), a twisted dipole or sigmoid (middle), and a twisted quadrupole configuration (bottom) are shown, in form of a magnetogram (grey scale background images in left panels) and in form of extrapolated magnetic field lines, calculated with the *vertical current approximation nonlinear force-free field (VCA-NLFFF)* code (Aschwanden 2013)

(Yan et al. 2012), the M2.9 flare on 2010 October 16 in NOAA 11112 (Kumar et al. 2013), the X2.1 flare on 2011 September 3 in NOAA 11283 (Ruan et al. 2014), and the CME eruptions in AR 12158 (Vemareddy et al. 2016). A rotation-related flare occurs generally when the rotation rate of the sunspot reaches its maximum (Li and Liu 2015). However, rapid rotation is not always required, while shearing motion can be sufficient to account for the energetics and helicity content for some major flares also (Kazachenko et al. 2010). On one occasion, the sunspot rotation was observed to be reversed during an X1.6 flare, which may be caused by a change of the Lorentz torque in response to shrinkage of the coronal field during the flare (Bi et al. 2016). A high correlation between the sunspot rotation speed and the change in the total accumulated helicity is found, and the net current shows a synchronous change with the sunspot rotation rate (Wang et al. 2016)

On the theoretical side, the most common interpretation attributes the sunspot rotation to injection of helical twist into the corona, producing sigmoid-shaped dipolar configurations, which are more likely to lead to flaring and eruption of CMEs than untwisted active regions. Numerical MHD simulations of rotating sunspots with inflows from a magnetic pore were attempted to test whether flare triggering via kink instability occurs (Gerrard et al. 2003). 3-D MHD simulations of an emerging twisted magnetic flux tube from the convection zone (Fan 2009; Santos et al. 2011; Török et al. 2013; Sturrock et al. 2015; Sturrock and Hood 2016) show that significant rotational motion sets in within each magnetic polarity, producing a sigmoid-shaped, dipped core field in the corona. The rotational motion in the two polarities is a result of propagation of nonlinear torsional Alfvén waves along the flux tube, which transports significant twist from the tube's interior portion toward its expanded coronal portion, ultimately leading to eruption (Fan 2009). The flare/CME trigger in a rotating sunspot environment is conveyed by a horizontal Lorentz force, which can explain the connections between the rapid and irreversible photospheric vector magnetic field change and the observed short-term motions associated with a flare. In particular, the unbalanced torque provided by the horizontal Lorentz force change can explain the measured angular acceleration (Wang et al. 2014; Sturrock et al. 2015; Sturrock and Hood 2016). Magnetic modeling (with NLFFF codes) show that the evolution of an active region can be approximated by a time series of force-free equilibria, but when the sigmoid-shaped field exceeds a critical twist, this leads to a loss of equilibrium and can trigger the onset of multiple eruptions (Vemareddy et al. 2016). The free energy that is available for dissipation during a flare/CME event can directly be calculated with the *vertical current approximation nonlinear force free field (VCA-NLFFF)* code (Fig. 4.19), which takes the helical twist of rotating sunspots due to vertical currents into account (Aschwanden 2013).

4.9 Sunspot Light Bridges

A short description of light bridges is given in the review on the magnetic structure of sunspots (Borrero and Ichimoto 2011). Since the umbra of a sunspot is dominated by strong magnetic fields, convection is generally inhibited in the umbra, which is the reason why no granulation is visible in the umbra. However, when a sunspot decays, the magnetic field strength becomes weaker and magneto-convection takes over, which leads to the features of *umbral dots* and *light bridges*, both being manifestations of convection inside the umbra. Light bridges are usually seen along "fissures" where a sunspot forms or decays. Light bridges are elongated bright features that often split the umbra into two (or more) sections, connecting two different sides of the penumbra (Fig. 4.20). Light bridges and umbral dots share many similarities, for instance both feature a central dark lane and bright edges. Light bridges can be considered as an extreme form of elongated umbral dots. The larger size of light bridges allows the detection of both blue and redshifted velocities with arc-second resolution. Observations with sub-arcsecond resolution

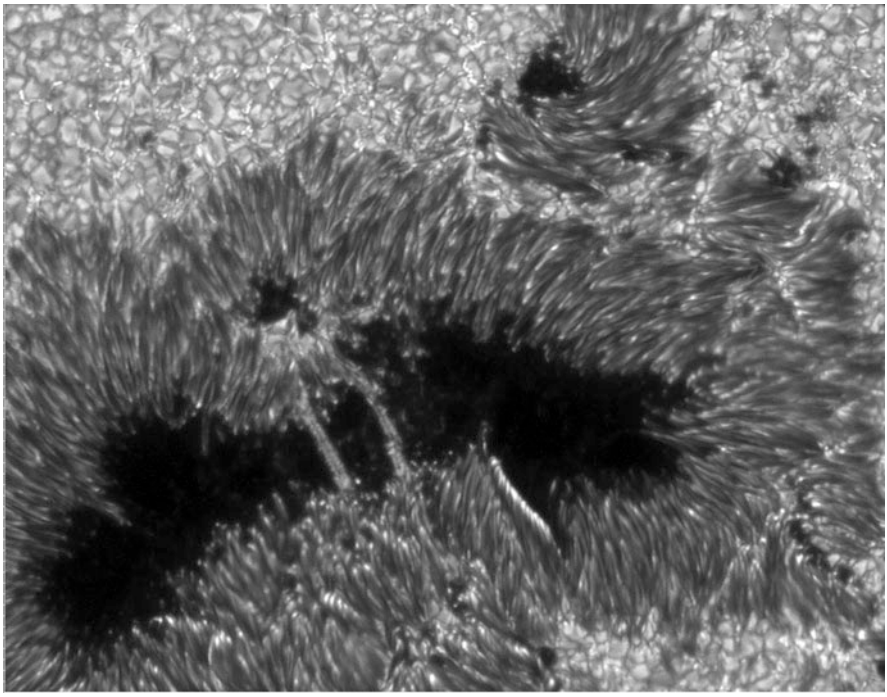

Fig. 4.20 This sunspot image, observed with the Swedish Vacuum Solar Telescope (SVST) on 2000 May 22 (using adaptive optics), shows two so-called *white-light bridges* during the decay phase of a large sunspot, extending over 5000 km and connecting the north and south umbral regions. As days progressed, the light bridge expanded to fill the void as the sunspots moved apart and decayed (Credit: G. Scharmer, L. Rouppe van der Voort, SVST)

clearly establish a connection between upflows and the central dark lane in light bridges, as well as between downflows and the bright edges of the light bridge, similar to the convective flow pattern in granulation cells outside the penumbra (Hirzberger et al. 2002; Berger and Berdyugina 2003; Rouppe van der Voort et al. 2010). Moreover, the magnetic field is weaker and slightly more inclined in light bridges than in the surrounding umbra, as it occurs in umbral dots also (Jurcak et al. 2006).

The formation process and evolution of light bridges in sunspots is not fully understood. Observations show evidence for plasma ejections along a light bridge of a stable and mature sunspot, in form of Hα surges as well as EUV jets at 171 Å, which could be a by-product of a magnetic reconnection process (Asai et al. 2001). Evidence for plasma ejection from a light bridge followed by Ellerman bombs, with opposite polarities in the light bridge with respect to the umbra, was interpreted also in terms of low-altitude magnetic reconnection, as a result of magnetic cancellation in the photosphere (Bharti et al. 2007). More jets ejected from a sunspot light bridge are reported in Liu (2012), Robustini et al. (2016), and Song et al. (2017). The formation process of a light bridge could be traced for several days with unprecedented resolution with SOT/Hinode (Katsukawa et al. 2007), finding that many umbral dots were observed to be emerging from the leading edges of penumbral filaments and rapidly intruding into the umbra. They found that the light bridges and the umbral dots had significantly weaker magnetic fields associated with upflows relative to the core of the umbra, which implies that there is hot gas with weak field strength penetrating from the subphotosphere to near the visible surface. They suggest that the emergence and the inward motion are triggered by a buoyant flux tube as well as subphotospheric flow crossing the sunspot (Katsukawa et al. 2007). Moreover, 3-D radiative MHD numerical simulations demonstrate that nearly field-free upflow plumes and umbral dots are a natural consequence of magneto-convection in an initially monolithic magnetic flux tube, and thus does not require the adoption of a cluster model to match the observed umbral dots (Schüssler and Vögler 2006).

Similarly, from SVST data it was concluded that the photospheric blue and redshifts observed in a granular light bridge are caused by the emergence of a small-scale, flat Ω-loop with highly inclined footpoints of opposite polarity that brings new magnetic field to the surface, which was the first time that magnetic flux was observed to emerge in the strongly magnetized environment of sunspots, pushed upwards by the convective flows of a granular light bridge (Louis et al. 2015). Lagg et al. (2014) find close similarities between Quiet-Sun granules and light bridge (Fig. 4.21), which points to the deep anchoring of granular light bridges in the underlying convection zone. The fast supersonic downflows in light bridge granules are most likely a result of invigorated convection due to radiative cooling into the neighboring umbra and the sampling of deeper layers adjacent to the slanted walls of the Wilson depression (Lagg et al. 2014).

Doppler shift analysis of SOT/Hinode observations reveal nonuniform flows with peak velocities of 250 and 180 m s^{-1} (Louis et al. 2008), supersonic downflows in light bridges with velocities of up to 10 km s^{-1}, which are the strongest photospheric

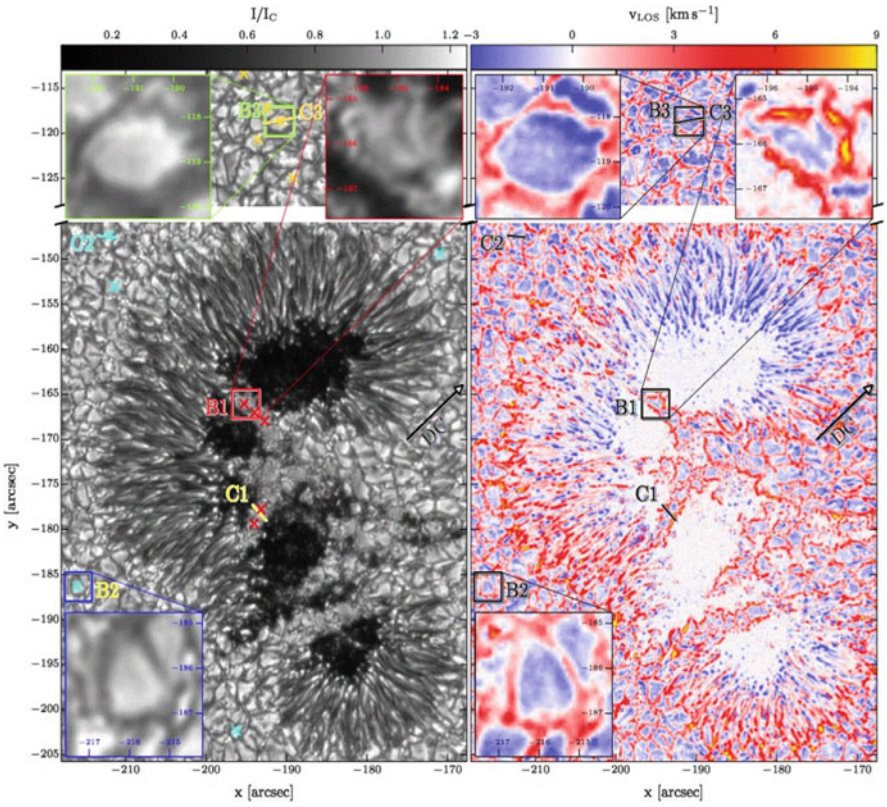

Fig. 4.21 Continuum map of AR 10926 of Stokes I (left) and line-of-sight velocity map (right; with red and blueshifts). The 3 boxes contain locations in light bridges (B1, C1) and in the Quiet Sun. Note the similar convection patterns in all 3 boxes (Lagg et al. 2014)

flows ever measured in light bridges (Louis et al. 2009; Shimizu 2011). IBIS data reveal downward velocities of 200 m s^{-1} in pores, and 150 m s^{-1} in the light bridge of a pore, which is consistent with the velocity structure of a convective roll (Giordano et al. 2008).

The global 5-min oscillations of the Sun exhibit interesting properties in sunspots with light bridges. The 5-min oscillations are suppressed in the umbra, while the 3-min oscillations occupy all cores of the sunspot umbra separated by light bridges (Fig. 4.21), and thus may either not be affected by umbral oscillations or share the same source (Yuan et al. 2014). Some sunspot light bridges exhibit oscillating light walls, probably excited by p-mode leakage from below the photosphere (Yang et al. 2015). Some light bridges were found to exhibit not only 5-min periods, but also persistent sub-minute oscillations (Yuan and Walsh 2016), or surge-like, intermittent pulses, probably excited by upward propagating slow-mode shocks (Zhang et al. 2017).

A first numerical simulation of flux emergence and accompanying light bridge formation was undertaken by Toriumi et al. (2015b), based on data of an active region that is likely to be produced by magnetic reconnection driven by magneto-convective evolution (Toriumi et al. 2015a). The convective upflow continuously transports horizontal fields to the surface layer and creates a light bridge structure.

4.10 Photospheric Waves and Oscillations

Helioseismology studies waves and oscillations in the solar interior but are detected on the solar surface (photosphere), a rich field that started after the discovery of the global 5-min oscillations in the 1970's. Coronal seismology, on the other hand, investigates standing and propagating waves and oscillations in the solar corona, which was initiated after the discovery of fast kink-mode oscillations in TRACE EUV movies in 1998. Expanding the discovery space of waves and oscillation phenomena in spatial and wavelength domains, we could envision "photo-seismology" and "chromo-seismology" for the two domains of the photosphere and chromosphere, but nobody has used these terms yet. Nevertheless, since the photosphere and the chromosphere are "sandwiched" between the solar interior and the corona, it is naturally expected that many of the helioseismic and coronal waves couple in upward and downward direction with structures seen in the photosphere and chromosphere. Consequently, we expect to see at least 4 different types of waves and oscillations in the photosphere: (i) coupled waves of the helioseismic global 5-min oscillations, also called p-mode leakage, (ii) coupled waves of fast and slow MHD modes from oscillating loops in the solar corona, and (iii) global spherically propagating waves in photospheric heights, also called running penumbral waves, and (iv) Moreton-Ramsey waves (observed in Hα wavelengths), chromospheric (or upper photospheric) signatures of large-scale global shock waves.

(i) The 5-min umbral oscillations are coherent amplifications with large spatial scales (typically a substantial fraction of the entire umbra), with periods of 4–7 min, and rms velocity amplitudes of 40–90 m s^{-1}, observed in lines that form in the low photosphere. There are also 3-min umbral oscillations of smaller spatial scales (3″–4″), observed in lines that form in the upper photosphere and chromosphere, with periods of order 2–3 min, and amplitudes of a few 100 m s^{-1}. The 5-min p-mode oscillations are believed to leak out of the photosphere and to propell spicules into chromospheric heights (De Pontieu et al. 2004). The photospheric velocity field and intensities are dominated by granular convection and p-modes. De Pontieu et al. (2004, 2005) demonstrated that the p-modes leak sufficient energy, on inclined magnetic flux tubes, from the global resonant cavity into the chromosphere, to power shocks that drive upward flows and form spicules. The nonverticality of the flux tube increases the acoustic cutoff period to values closer to the dominant periods of the photospheric oscillations, thus allowing tunneling or even direct propagation

into the corona (De Pontieu et al. 2005). Chromospheric velocity oscillations show a 3-min period with a clear sawtooth shape typical of propagating shock wave fronts, while photospheric velocity oscillations have basically a 5-min period, although the power spectrum shows a secondary peak in the 3-min band also (Centeno et al. 2006). The most recent observations with the *Fast Imaging Solar Spectrograph (FISS)* of the 1.6 m *Goode New Solar Telescope (NST)* clearly demonstrates the photospheric origin of 3-min oscillations (Fig. 4.22) in the photospheric Ni I (5436 Å), Fe I (5435 Å), and Na I D_2 5980 Å) lines (Chae et al. 2017). Photospheric oscillations were also detected in the infrared line 15,650 Å, which is sensitive to magnetic field oscillations (Bellot Rubio et al. 2000). MHD simulations of magneto-acoustic wave propagation from the photosphere to the low chromosphere show that the fast (magnetic) mode in the region $c_s < v_A$ does not reach the chromosphere and reflects back to the photosphere at a somewhat higher layer than the $c_s = v_A$ line (Khomenko and Collados 2006; Khomeno et al. 2008). This behavior is due to wave refraction, caused primarily by the vertical and horizontal gradients of the Alfvén speed. The slow (acoustic) mode continues up to the chromosphere along the magnetic field lines with increasing amplitude, which generates a wide range of periods at different distances from the sunspot axis (Khomenko and Collados 2006). Waves with

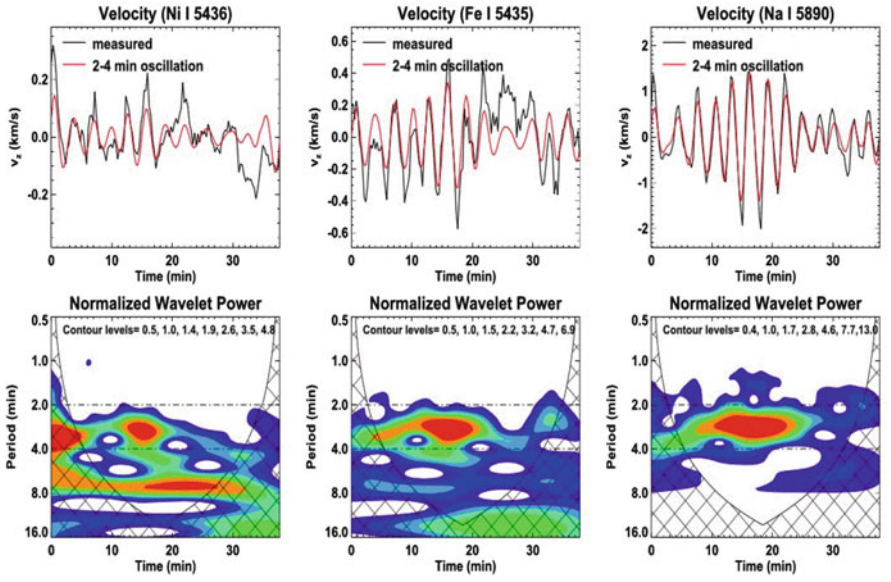

Fig. 4.22 Velocity oscillations (top panels) and wavelet periods (bottom panels) observed in a sunspot umbrae on 2015 June 16 with the *Fast Imaging Solar Spectrograph (FISS)* of the 1.6 m *Goode New Solar Telescope (NST)* in the photospheric Ni I (5436 Å), Fe I (5435 Å), and Na I D_2 5980 Å) lines (Chae et al. 2017)

frequencies above the acoustic cut-off propagate from the photosphere to the upper layers only in restricted areas of the Quiet Sun, a large fraction of the quiet chromosphere is occupied by "magnetic shadows", surrounding network regions, detected in the Ca II line (Vecchio et al. 2007). From IRIS observations (in the chromosphere and upper photosphere) a positive correlation was found between the maximum velocity and deceleration, a result that is consistent with numerical simulations of upward propagating magneto-acoustic shock waves (Tian et al. 2014). Some p-mode waves have been traced from the photosphere through the chromosphere all the way up into the corona via cross-correlation and time-distance helioseismic analysis (Zhao et al. 2016). Waves in different frequencies are found to travel along different paths (Zhao et al. 2016). In network regions, besides p-mode leakage as origin of photospheric oscillations, alternative mechanisms in terms of mode conversion, or reflection and refraction of waves on the magnetic canopy, have also been considered (Kontogiannis et al. 2010).

(ii) Fast kink-mode oscillations of coronal loops show periods in a typical range of $P \approx 2$–10 min, which depends on the loop length L and Alfvén velocity (v_A), or the tube speed c_k,

$$P_{kink} = \frac{2L}{c_k} = \frac{2L}{v_A}\left(1 + \frac{(\rho_e/\rho_0)}{2}\right)^{1/2}, \tag{4.10.1}$$

with ρ_e and ρ_0 the external and internal electron density, respectively. While the fast kink-mode displays the largest oscillating amplitude in the midpoint in transverse direction to the loop axis, the amplitude is substantially reduced near the photospheric footpoints of the loops, but might still be detectable in some wave phenomena coupled to photospheric features. It was proposed that some oscillating loops are so sensitive to the source position of wave excitation, so that rocking motions of the photospheric plasma associated with some flares cause a few loops to oscillate in (anti)phase in the fundamental mode, with a period and decay rate that are determined largely by the characteristics of the photosphere, rather than by the corona (Schrijver and Brown 2000). A coupling between oscillating microwave-emitting loops and p-mode oscillations leakage in a sunspot was found for a number of flare events, with periods around ≈ 3 min (Sych et al. 2009). Based on SOT/Hinode (Fujimura and Tsuneta 2009), ROSA (Morton et al. 2011; Grant et al. 2015; Freij et al. 2016), and with *Dutch Open Telescope (DOT)* (Freij et al. 2016) observations, both longitudinal (sausage-mode) and transverse (kink-mode) MHD waves were detected in photospheric fluxtubes.

(iii) Running penumbral waves are coherent outward-propagating wave fronts (with subtended angles of 90°–270°) readily observed in the penumbral chromosphere. The measured radial phase speeds vary in the range of 8–35 km s^{-1}, with a tendency of decreasing phase speed with distance. Recent studies have confirmed that running penumbral waves have the same nature as umbral flashes, both being slow-mode magneto-acoustic waves that propagate upward

and are guided by the inclined magnetic field of the penumbra (Bloomfield et al. 2007; Jess et al. 2013; Löhner-Böttcher and Bello Gonzalez 2015; Löhner-Böttcher et al. 2016). This magnetic field inclination increases from the inner to the outer penumbra, causing an increasing path length that appears as an outward propagation with decreasing velocity.

(iv) Moreton-Ramsey waves are also known as fast-mode MHD waves, which propagate globally along the spherical solar surface. STEREO observations determined altitude ranges of $\lesssim 0.15 R_\odot$ and speeds of $\approx$ 500–1500 km s^{-1} for these waves, generated in conjunction with large flares and CMEs. Other flare-related phenomenona with global propagation characteristics are the "sunquakes", first discovered by Kosovichev and Zharkova (1998), which are usually detected during the impulsive phase of the largest (M- and X-class) flares, but occasionally also in weak C-class flares (Sharykin et al. 2015), and is analyzed with helioseismic methods (e.g., Martinez-Oliveros et al. 2008). Helioseismic waves are believed to be initiated by the photospheric impact of electron (or proton) beams accelerated in the early impulsive phase of flares (e.g., Kosovichev 2007).

References

(4.1) Solar Diameter and Oblateness

Damiani, C., Rozelot, J.P., Lefebvre, S. et al. 2011, *A brief history of the solar oblateness. A review*, J.Atmos Solar-Terr. Phys. 73, 241, [24 c, 4 c/y].

Emilio, M., Kuhn, J.R., Bush, R.I., and Scholl, I.F. 2012, *Measuring the solar radius from space during the 2003 and 2006 Mercury transits*, ApJ 750, 135, [24 c, 4 c/y].

Emilio, M., Couvidat, S., Bush, R. I., et al. 2015, *Measuring the Solar Radius from Space during the 2012 Venus Transit*, ApJ 798, 48, [4 c, 2 c/y].

Fivian, M.D., Hudson, H.S., Lin, R.P. and Zahid, H.J. 2008, *A large excess in apparent solar oblateness due to surface magnetism*, Science 322, 560, [32 c, 3 c/y].

Gough, D. 2012, *How oblate is the Sun?*, Science 337, 1611, [9 c, 2 c/y].

Kosovichev, A. and Rozelot, J.P. 2018a, *Cyclic changes of the Sun's seismic radius*, ApJ 861, 90, [1 c, 1 c/y].

Kosovichev, A. and Rozelot, J.P. 2018a, *Solar cycle variations of rotation and asphericity in the near-surface shear layer*, JASTP 176, 21, [1 c, 1 c/y].

Kuhn, J.R., Bush, R., Emilio, M., and Scholl, I.F. 2012, *The precise solar shape and its variability*, Science 337, 1638, [26 c, 5 c/y].

Rozelot, J.P., Kosovichev, A., and Kilcik, A. 2015, *Solar radius variations: An inquisitive wavelength dependence*, ApJ 812, 91, [5 c, 2 c/y].

Wachter, R., Schou, J., Rabello-Soares, M.C. et al. 2012, *Image quality of the HMI onboard the SDO*, SoPh 275, 261, [35 c, 6 c/y].

(4.2) Magnetic Flux Distribution

Close, R.M., Parnell, C.E., Longcope, D.W. et al. 2004, *Recycling of the solar corona's magnetic field*, ApJ 612, L81, [52, 4 c/y].

Fragos, T., Rantsiou, E., and Vlahos, L. 2004, *On the distribution of magnetic energy storage in solar active regions* A&A 420, 719, [15 c, 1 c/y].

Hagenaar, H.J. 2001, *Ephemeral regions on a sequence of full-disk MDI magnetograms*, ApJ 555, 448, [152 c, 9 c/y].

Kitiashvili, I.N., Kosovichev, A.G., Wray, A.A., et al. 2010, *Mechanism of spontaneous formation of stable magnetic structures on the Sun*, ApJ 719, 307, [64 c, 9 c/y].

Mandrini, C.H., Démoulin, P., and Klimchuk, J.A. 2000, *Magnetic field and plasma scaling laws: Implications for coronal heating models*, ApJ 530, 999, [138 c, 8 c/y].

Okamoto, T. and Sakurai T. 2018, *Super-strong magnetic field in sunspots*, ApJ 852, L16.

Parnell, C.E. 2002, *Nature of the magnetic carpet. - I. Distribution of magnetic fluxes*, MNRAS 335, 389. [43 c, 3 c/y].

Parnell, C.E., DeForest, C.E., Hagenaar, H.J. et al. 2009, *A power-law distribution of solar magnetic fields over more than five decades in flux*, ApJ 698, 75, [10 c/y, 86 c].

Schrijver, C.J., Title, A.M., van Ballegooijen, A.A., et al. (1997), *Sustaining the quiet photospheric network: The balance of flux emergence, fragmentation, merging, and cancellation*, ApJ 487, 424, [289 c, 14 c/y].

Stenflo, J.O. 2012, *Scaling laws for magnetic fields on the Quiet Sun*, A&A 541, A17, [29 c, 5 c/y].

Wiegelmann, T. and Solanki, S.K. 2004, *Similarities and differences between coronal holes and the Quiet Sun: Are loop statistics the key?* SoPh 225, 227, [34 c, 3 c/y].

(4.3) Bimodal Magnetic Area Distributions

Baumann, I. and Solanki, S.K. 2005, *On the size distribution of sunspot groups in the Greenwich sunspot record 1874–1976*, A&A 443, 1061, [37 c, 3 c/y].

Jiang, J., Cameron, R.H., Schmitt, D. and Schüssler, M. 2011, *The solar magnetic field since 1700. I. Characteristics of sunspot group emergence and reconstruction of the butterfly diagram*, A&A 528, A82, [38 c, 6 c/y].

Nagovitsyn, Y.A., Pevtsov, A.A. and Livingston, W.C. 2012, *On a possible explanation of the long-term decrease in sunspot field strength*, ApJ 758, L20, [43 c, 8 c/y].

Meunier, N. 2003, *Statistical properties of magnetic structures: Their dependence on solar scale and solar activity*, A&A 405, 1107, [38 c, 3 c/y].

Munoz-Jaramillo, A., Senkpeil, R.R., Windmueller, J.C. et al. 2015, *Small-scale and global dynamos and the area and flux distributions of active regions, sunspot groups, and sunspots: A multi-database study*, ApJ 800, 48, [15 c, 6 c/y].

Parnell, C.E., DeForest, C.E., Hagenaar, H.J. et al. 2009, *A power-law distribution of solar magnetic fields over more than five decades in flux*, ApJ 698, 75, [86 c, 10 c/y].

Schad, T.A. and Penn, M.J. 2010, *Structural invariance of sunspot umbrae over the Solar Cycle: 1993–2004*, SoPh 262, 19, [19 c, 3 c/y].

Tlatov, A.G. and Pevtsov, A.A. 2014, *Bimodal distribution of magnetic fields and areas of sunspots*, SoPh 289, 1143, [18 c, 5 c/y].

Zhang, J., Wang, Y., and Liu, Y. 2010, *Statistical properties of solar active regions obtained from an automatic detection system and the computational bias*, ApJ 723, 1006, [26 c, 3 c/y].

Zharkov, S., Zharkova, V.V. and Ipson, S.S. 2005, *Statistical properties of sunspots in 1996–2004: I. Detection, north south asymmetry and area distribution*, SoPh 228, 377, [34 c, 3 c/y].

(4.4) The Multi-Fractal Photosphere

Balke, A.C., Schrijver, C.J., Zwaan,C., et al. 1993, *Percolation theory and the geometry of photospheric magnetic flux concentrations*, SoPh 143, 215 [43 c, 2 c/s].

Berrilli, F., Del Moro, D., Russo, S., et al. 2005, *Spatial clustering of photospheric structures*, ApJ 632, 677, [23 c, 2 c/s].
Bovelet, B. and Wiehr, E. 2001, *A new algorithm for pattern recognition and its application to granulation and limb faculae*, SoPh 201, 13, [41 c, 2 c/y].
Cadavid, A.C., Lawrence, J.K., Ruzmaikin, A., et al. 1994, *Multifractal models of small-scale magnetic fields*, ApJ 429, 391, [26 c, 1 c/y].
Conlon, P.A., Gallagher, P.T., McAteer, R.T.J., et al. 2008, *Multifractal properties of evolving active regions*, SoPh 248, 297, [41 c, 4 c/y].
Gallagher, P.T., Phillips, K.J.H., Harra-Murnion, L.K., et al. 1998, *Properties of the Quiet Sun EUV network*, A&A 335, 733, [65 c, 3 c/y].
Georgoulis, M.K., Rust, D.M., Bernasconi, P.N., et al. 2002, *Statistics, morphology, and energetics of Ellerman bombs*, ApJ 575, 506, [119 c, 8 c/y].
Hathaway, D.H., Beck, J.G., Bogart, R.S., et al. 2000, *The photospheric convection spectrum* SoPh 193, 299, [99 c, 6 c/y]. s
Hirzberger, J., Vazquez, M., Bonet, J.A., et al. 1997, *Time series of solar granulation images. I. Differences between small and large granules in quiet regions*, ApJ 480, 406, [72 c, 4 c/y].
Janssen, K., Voegler, A., and Kneer, F. 2003, *On the fractal dimension of small-scale magnetic structures in the Sun*, A&A 409, 1127, [42 c, 3 c/y].
Lawrence, J.K. 1991, *Diffusion of magnetic flux elements on a fractal geometry*, SoPh 135, 249, [32 c, 1 c/y].
Lawrence, J.K. and Schrijver, C.J. 1993, *Anomalous diffusion of magnetic elements across the solar surface*, ApJ 411, 402, [50 c, 2 c/y].
Lawrence, J.K., Ruzmaikin, A., and Cadavid, A.C. 1993, *Multifractal measure of the solar magnetic field*, ApJ 417, 805, [77 c, 3 c/y].
Lawrence, J.K., Cadavid, A.C., and Ruzmaikin, A.A. 1996, *On the multifractal distribution of solar magnetic fields*, ApJ 465, 425, [25 c, 1 c/y].
Mandelbrot, B.B. 1977, *Fractals: form, chance, and dimension*, Translation of *Les objects fractals*, W.H. Freeman, San Francisco, [569 c, 14 c/y].
McAteer, R.T.J., Gallagher, P.T., and Ireland, J. 2005, *Statistics of active region complexity. A Large-scale fractal dimension survey*, ApJ 662, 691, [63 c, 5 c/y].
Meunier, N. 1999, *Fractal analysis of Michelson Doppler Imager magnetograms: a contribution to the study of the formation of solar active regions.* ApJ 515, 801, [42 c, 2 c/y].
Meunier, N. 2004, *Complexity of magnetic structures: flares and cycle phase dependence*, A&A 420, 333, [17 c, 1 c/y].
Paniveni, U., Krishan, V., Sing, J., et al. 2005, *On the fractal structure of solar supergranulation*, SoPh 231, 1, [8 c, 0.6 c/y].
Rieutord, M., Meunier, N., Roudier, T., et al. 2008, *Solar supergranulation revealed by granule tracking*, A&A 479, L17, [32 c, 3 c/y].
Rieutord, M., Roudier, T., Rincon, F., 2010, *On the power spectrum of solar surface flows*, A&A 512, A4, [37 c, 5 c/y].
Roudier, T. and Muller, R. 1986, *Structure of solar granulation*, SoPh 107, 11, [93 c, 3 c/y].

(4.5) Mini-Granulation

Abramenko, V.I., Yurchyshyn, V.B., Goode, P.R., et al. 2012, *Detection of small-scale granular structures in the Quiet Sun with the New Solar Telescope*, ApJ 756, L27, [16 c, 3 c/y].
Aschwanden, M.J., Scholkmann, F., Béthume, W., et al. 2018, *Order out of randomness: Self-organization processes in astrophysics*, SSRv 214, 55.
Chandrasekhar, S. 1961, *Hydrodynamic and hydromagnetic Stability*, Clarendon Press, Oxford.
Krishan, V. 1991, *A model of solar granulation through inverse cascade*, MNRAS 250, 50, [20 c, 0.8 c/y].
Lorenz, E.N. 1963, *Deterministic nonperiodic flow*, J. Atmos. Sciences 20, 130, [4983 c, 91 c/y].

Schuster, H.G. 1988, *Deterministic Chaos*, VCH Verlag: Weinheim.
Van Kooten, S.J. and Cranmer, S.R. 2017, *Characterizing the motion of solar magnetic bright points at high resolution*, ApJ 850, 64, [1 c, 1 c/y].

(4.6) Quiet-Sun and Polar Fields

de Wijn, A.G., Stenflo, J.O., Solanki, S.K., et al. 2009, *Small-scale solar magnetic fields*, SSRv 144, 275, [116 c, 14 c/y].
Dikpati, M. and Charbonneau, P. 1999, *A Babcock-Leighton flux transport dynamo with solar-like differential rotation*, ApJ 518, 508, [478 c, 26 c/y].
Dominquez Cerdena, I., Sanchez, A., and Kneer, F. 2003, *Inter-network magnetic fields observed with sub-arcsec resolution*, A&A 407, 741, [96 c, 7 c/y].
Harvey, J.W., Branston, D., Henney, C.J., et al. 2007, *Seething horizontal magnetic fields in the quiet solar photosphere*, ApJ 659, L177, [98 c, 9 c/y].
Lagg, A., Lites, B., Harvey, J., et al. 2017, *Measurements of photospheric and chromospheric magnetic fields*, SSRv 210, 37, [6 c, 6 c/y].
Lin, H.S. and Rimmele, T. 1999, *The granular magnetic fields of the Quiet Sun*, ApJ 514, 448, [166 c, 9 c/y].
Lites, B.W., Leka, K.D., Skumanich, A., et al. 1996, *Small-scale horizontal magnetic fields in the solar photosphere*, ApJ 460, 1019, [131 c, 6 c/y].
Lites, B.W., Kubo, M., Socas-Navarro, H., et al. 2008, *The horizontal magnetic field flux of the Quiet-Sun internetwork as observed with the Hinode Spectro-Polarimeter*, ApJ 672, 1237, [309 c, 33 c/y].
Stenflo, J.O. 2004, *Solar physics: Hidden magnetism*, Nature 430, 304, [19 c, 1 c/y].
Stenflo, J.O. 2012, *Scaling laws for magnetic fields on the Quiet Sun*, A&A 541, A17, [29 c, 5 c/y].
Tsuneta, S., Ichimoto, K., Katsukawa, Y., et al. 2008, *The magnetic landscape of the Sun's polar region*, ApJ 688, 1374, [114 c, 12 c/y].
Wang, Y.M., Nash, A.G., and Sheeley, N.R.Jr. 1989, *Magnetic flux transport on the Sun*, Science 245, 712, [216 c, 8 c/y].

(4.7) Penumbral Dynamics

Borrero, J.M. and Ichimoto, K. 2011, *Magnetic structure of sunspots*, LRSP 8, 4, [67 c, 10 c/y].
Choudhary, D.P. and Beck, C. 2018, *Thermodynamic properties of the inverse Evershed flow at its downflow points*, ApJ 859, 139.
Rempel, M., Schüssler, M., Cameron, R.H., et al. 2009, *Penumbral Structure and Outflows in Simulated Sunspots*, Science, 325, 171, [135 c, 16 c/y].
Rempel, M. 2011, *Penumbral fine structure and driving mechanisms of large-scale flows in simulated sunspots*, ApJ 729, 5, [64 c, 10 c/y].
Rempel, M. and Schlichenmaier, R. 2011, *Sunspot modeling: From simplified models to radiative MHD simulations*, LRSP 8, 3, [35 c, 5 c/y].
Scharmer, G.B., Henriques, B.M.H., Kiselman, D. et al. 2011, *Detection of convective downflows in a sunspot penumbra*, Science, 333, 316, [50 c, 8 c/y].
Schlichenmaier, R., Jahn, K., and Schmidt, H.U. 1998, *Magnetic flux tubes evolving in sunspots. A model for the penumbral fine structure and the Evershed flow*, A&A 337, 897, [162 c, 8 c/y].
Solanki, S.K. and Montavon, C.A.P. 1993, *Uncombed fields as the source of the broad-band circular polarization of sunspots*, A&A 275, 283, [215 c, 9 c/y].
Solanki, S.K. 2003, *Sunspots: An overview*, A&ARv 11/2, 153, [387 c, 27 c/y].

Spruit, H.C. and Scharmer, G.B. 2006, *Fine structure, magnetic field and heating of sunspot penumbrae*, A&A 447, 343. [132 c, 11 c/y].
Thomas,J.H., Weiss, N.O., Tobias, S.M. et al. 2002, *Downward pumping of magnetic flux as the cause of filamentary structures in sunspot penumbrae*, Nature 420, 390, [86 c, 6 c/y].
Thomas, J.H. and Weiss, N.O. 2004, *Fine structure in sunspots*, ARvAA 42, 517, [85 c, 4 c/y].
Thomas, J.H. and Weiss, N.O. 2008, *Sunspots and starspots*, Cambridge, UK: Cambridge Unviersity Press, [61 c, 6 c/y].

(4.8) Rotating Sunspots

Aschwanden, M.J. 2013, *A nonlinear force-free magnetic field approximation suitable for fast forward-fitting to coronal loops*, SoPh 287, 323, [17 c, 4 c/y].
Bi, Y., Jiang, Y., Jang, J., et al. 2016, *Observation of a reversal of rotation in a sunspot during a solar flare*, Nature Communications 7, 13798, [6 c, 4 c/y].
Brown, D.S., Nightingale, R.W., Alexander, D., et al. 2003, *Observations of rotating sunspots from TRACE*, SoPh 216, 79, [144 c, 10 c/y].
Evershed, J. 1910, *Radial movement in sun-spots (Second paper)*, MNRAS 70, 217, [48 c, 0.4 c/y].
Fan, Y. 2009, *The emergence of a twisted flux tube into the solar atmosphere: Sunspot rotations and the formation of a coronal flux rope*, ApJ 697, 1529, [94 c, 11 c/y].
Gerrard, C.L., Brown, D.S., Mellor, C., et al. 2003, *MHD simulations of sunspot rotation and the coronal consequences*, SoPh 213, 39, [11 c, 0.8 c/y].
Hiremath, K.M. 2002, *Change of rotation rates of sunspot groups during their lifetimes: Clues ot the sites of origin of different flux tubes*, A&A 386, 674, [24 c, 2 c/y].
Jain, K., Komm, R.W., Gonzalez-Hernandez, I. et al. 2012, *Subsurface flows in and around active regions with rotating and non-rotating sunspots*, SoPh 279, 349, [9 c, 2 c/y].
Jiang, Y., Zheng, R., Yang, J., et al. 2012, *Rapid sunspot rotation associated with the X2.2 flare on 2011 February 15*, ApJ 744, 50, [43 c, 8 c/y].
Kazachenko, M.D., Canfield, R.C., Longcope, D.W., et al. 2010, *Sunspot rotation, flare energetics, and flux rope helicity: The Halloween flare on 2003 October 28*, ApJ 722, 1539, [18 c, 2 c/y].
Kosovichev, A.G. 2002, *Subsurface structure of sunspots*, Astron.Nachrichten 323, 186, [28 c, 2 c/y].
Kumar, P., Park, S.H., Cho, K.S., et al. 2013, *Multiwavelength study of a solar eruption from AR NOAA 1112. I. Flux emergence, sunspot rotation, and triggering of a solar flare*, SoPh 282, 503, [15 c, 3 c/y].
Li, A. and Liu, Y. 2015, *Sunspot rotation and the M-class flare in solar active region NOAA 11158*, SoPh 290, 2199, [5 c, 2 c/y].
Min, S.Y. and Chae, J.C. 2009, *The rotating sunspot in AR 10930*, SoPh 258, 203, [46 c, 5 c/y].
Ruan, G., Chen, Y., Wang, S. et al. 2014, *A solar eruption driven by rapid sunspot rotation*, ApJ 784, 165, [20 c, 6 c/y].
Ruzdjak, D., Ruzdjak, V., Brajsa, R., et al. 2004, *Deceleration of the rotational velocities of sunspot groups during their evolution*, SoPh 221, 225, [18 c, 1 c/y].
Santos, J.C., Büchner, J. and Otto, A. 2011, *3D MHD simulations of electric current development in a rotating sunspot: Active region NOAA 8210*, A&A 535, A111, [9 c, 1 c/y].
Sturrock, Z., Hood, A.W., Archontis, V., et al. 2015, *Sunspot rotation. I. A consequence of flux emergence*, A&A 582, A76, [7 c, 3 c/y].
Sturrock, Z. and Hood, A.W. 2016, *Sunspot rotation. II. Effects of varying the field strength and twist of an emerging flux tube*, A&A 593, A63, [3 c, 2 c/y].
Török, T., Temmer, M., Valori, G., et al. 2013, *Initiation of coronal mass ejections by sunspot rotation*, SoPh 286, 453, [33 c, 7 c/y].
Tian, L. and Alexander, D. 2006, *Role of sunspot and sunspot-group rotation in driving sigmoidal active region eruptions*, SoPh 233, 29, [38 c, 3 c/y].

Vemareddy, P., Ambastha, A., and Maurya, R.A. 2012, *On the role of rotating sunspots in the activity of solar active region NOAA 11158*, ApJ 761, 60, [42 c, 8 c/y].
Vemareddy, P., Cheng, X., and Ravindra, B. 2016, *Sunspot rotation as a driver of major solar eruptions in NOAA active region 12158.* ApJ 829, 24, [9 c, 6 c/y].
Wang, S., Liu, C., Deng, N., et al. 2014, *Sudden photospheric motion and sunspot rotation associated with the X2.2 flare on 2011 February 15*, ApJ 782, L31, [25 c, 6 c/y].
Wang, R., Liu, Y.D., Wiegelmann, T., et al. 2016, *Relationship between sunspot rotation and a major solar eruption on 12 July 2012*, SoPh 291, 1159, [3 c, 2 c/y].
Yan, X.L. and Qu, Z.Q. 2007, *Rapid rotation of a sunspot associated with flares*, A&A 468, 1083, [37 c, 4 c/y].
Yan, X.L., Qu, Z.Q., and Xu, C.L. 2008, *A statistical study on rotating sunspots: Polarities, rotation directions, and helicities*, ApJ 682, L65, [33 c, 3 c/y].
Yan, X.L., Qu, Z.Q., Kong, D.F., et al. 2012, *Sunspot rotation, sigmoidal filament, flare, and coronal mass ejection: The event on 2000 February 10*, ApJ 754, 16, [23 c, 4 c/y].
Zhang, J., Li, L., and Song, Q. 2017, *Interaction between a fast rotating sunspot and ephemeral regions as the origin of the major solar event on 2006 December 13*, ApJ 662, L35, [75 c, 7 c/y].
Zhang, Y., Liu, J., and Zhang, H. 2008, *Relationship between rotating sunspots and flares*, SoPh 247, 39, [50 c, 5 c/y].
Zhao, J.W. and Kosovichev, A.G. 2003, *Helioseismic observation of the structure and dynamics of a rotating sunspot beneath the solar surface*, ApJ 591, 446, [83 c, 6 c/y].
Zhu, C., Alexander, D., and Tian, L. 2012, *Velocity characteristics of rotation sunspots*, SoPh 278, 121, [7 c, 1 c/y].

(4.9) Sunspot Light Bridges

Asai, A., Ishii, T.T., and Kurokawa, H. 2001, *Plasma ejection from a light bridge in a sunspot umbra*, ApJ 555, L65, [62 c, 4 c/y].
Berger, T.E. and Berdyugina, S.V. 2003, *The observation of sunspot light-bridge structure and dynamics*, ApJ 589, L117, [33 c, 4 c/y].
Bharti, L., Rimmele, T., Jain, R., et al. 2007, *Detection of opposite polarities in a sunspot light bridge: Evidence of low-altitude magnetic reconnection*, MNRAS 376, 1291, [27 c, 3 c/y].
Borrero, J.M., and Ichimoto, K. 2011, *Magnetic structure of sunspots*, LRSP 8, 4, [67 c, 10 c/y].
Giordano, S., Berilli, F., Del Moro, D., et al. 2008, *The photospheric structure of a solar pore with a light bridge*, A&A 489, 747, [22 c, 2 c/y].
Hirzberger, J., Bonet, J.A., Sobotka, M. et al. 2002, *Fine structure and dynamics in a light bridge inside a solar pore*, A&A 383, 275, [33 c, 4 c/y].
Jurcak, J., Martinez Pillet, V., and Sobotka, M. 2006, *The magnetic canopy above light bridges*, A&A 453, 1079, [58 c, 5 c/y].
Katsukawa, Y., Yokoyama, T., Berger, T.E., et al. 2007, *Formation process of a light bridge revealed with the Hinode/SOT*, PASJ 59, S577, [38 c, 4 c/y].
Lagg, A., Solanki, S.K., van Noort, M., et al. 2014, *Vigorous convection in a sunspot granular light bridge*, A&A 568, A60, [26 c, 7 c/y].
Liu, S. 2012, *A coronal jet ejection from a sunspot light bridge*, PASA 29, 193, [6 c, 1 c/y].
Louis, R.E., Bayanna, A.R., Mathew, S.K., et al. 2008, *Dynamics of sunspot light bridges as revealed by high-resolution images from Hinode*, SoPh 252, 43, [32 c, 3 c/y].
Louis, R.E. Bellot Rubio, L.R., Mathew, S.K. and Venkatakrishnan, P. 2009, *Supersonic downflows in a sunspot light bridge*, ApJ 704, L29, [32 c, 4 c/y].
Louis, R.E., Bellot Rubio, L.R., de la Cruz Rodriquez J., et al. 2015, *Small-scale magnetic flux emergence in a sunspot light bridge*, A&A 584, A1, [9 c, 4 c/y].
Robustini, C., Leenaarts, J., de la Cruz Rodriquez, J., et al. 2016, *Fan-shaped jets above the light bridge of a sunspot driven by reconnection*, A&A 590, A57, [14 c, 9 c/y].

Rouppe van der Voort, L., Bellot Rubio, L.R., and Ortiz, A. 2010, *Upflows in the central dark lane of sunspot light bridges*, ApJ 718, L78, [24 c, 3 c/y].
Schüssler, M. and Vögler, A. 2006, *Magnetoconvection in a sunspot umbra*, ApJ 641, L73, [161 c, 14 c/y].
Shimizu, T. 2011, *long-term evolution of magnetic and dynamical properties in a sunspot light bridge*, ApJ 738, 83, [62 c, 7 c/y].
Song, D., Chae, J.C., Yurchyshyn, V. et al. 2017, *Chromospheric plasma ejections in a light bridge of a sunspot*, ApJ 835, 240, [5 c, 5 c/y].
Toriumi, S., Cheung, M.C.M., and Katsukawa, Y. 2015a, *Light bridge in a developing active region. I. Observation of light bridge and its dynamic activity phenomena*, ApJ 811, 137, [20 c, 8 c/y].
Toriumi, S., Cheung, M.C.M., and Katsukawa, Y. 2015b, *Light bridge in a developing active region. II. Numerical simulation of flux emergence and light bridge formation*, ApJ 811, 138, [15 c, 6 c/y].
Yang, S., Zhang, J., Jiang, F., et al. 2015, *Oscillating light wall above a sunspot light bridge*, ApJ 804, L27, [16 c, 6 c/y].
Yuan, D., Nakariakov, V.M., Huang, Z., et al. 2014, *Oscillations in a sunspot with light bridges*, ApJ 792, 41, [21 c, 6 c/y].
Yuan, D. and Walsh, R.W. 2016, *Abnormal oscillation modes in a waning light bridge*, A&A 594, A101, [7 c, 5 c/y].
Zhang, J., Tian, H., He, J., et al. 2017, *Surge-like oscillations above sunspots light bridges driven by magneoacoustic shocks*, ApJ 838, 2, [6 c, 6 c/y].

(4.10) Photospheric Waves and Oscillations

Bellot Rubio, L.R., Collados, M., Ruiz Cobo, B., et al. 2000, *Oscillations in the photosphere of a sunspot umbra from the inversion of infrared Stokes profiles*, ApJ 534, 989, [55 c, 3 c/y].
Bloomfield, D.S., Lagg, A., and Solanki, S.K. 2007, *The nature of running penumbral waves revisited*, ApJ 671, 1005, [58 c, 6 c/y].
Centeno, R., Collados, M., Trujillo Bueno, J. 2006, *Spectro-polarimetric investigation of the propagation of magneto-acoustic waves and shock formation in sunspot atmospheres*, ApJ 640, 1153, [91 c, 8 c/y].
Chae, J., Lee, J., Cho, K., et al. 2017, *Photospheric origin of three-minute oscillations in a sunspot*, ApJ 836, 18, [6 c, 6 c/y].
De Pontieu, B., Erdelyi, R., James, S.P. 2004, *Solar chromospheric spicules from the leakage of photospheric oscillations and flows*, Nature 430, 536, [286 c, 21 c/y].
De Pontieu, B., Erdelyi, R., and De Moortel, I. 2005, *How to channel photospheric oscillations into the corona*, ApJ 624, L61, [124 c, 10 c/y].
Freij, N., Dorotovic, I., Morton, R.J., et al. 2016, *On the properties of slow MHD sausage waves within small-scale photospheric magnetic structures*, ApJ 817, 44, [7 c, 5 c/y].
Fujimura, D. and Tsuneta, S. 2009, *Properties of MHD waves in the solar photosphere obtained with Hinode*, ApJ 702, 1443, [63 c, 7 c/y].
Grant, S.D.T., Jess, D.B., Moreels, M.G., et al. 2015, *Wave damping observed in upward propagating sausage-mode oscillations contained within a magnetic pore*, ApJ 806, 132, [14 c, 6 c/y].
Jess, D.B., Reznikova, V.E., Van Doorsselaere, T. et al. 2013, *The influence of the magnetic field on running penumbral waves in the solar chromosphere*, ApJ 779, 168, [40 c, 9 c/y].
Khomenko, E. and Collados, M. 2006, *Numerical modeling of magnetohydrodynamic wave propagation and refraction in sunspots*, ApJ 653, 739, [89 c, 8 c/y].
Khomeno, E., Centeno, R., Collados, M., et al. 2008, *Channeling 5-minute photospheric oscillations into the solar outer atmosphere through small-scale vertical magnetic flux tubes*, ApJ 676, L85, [55 c, 6 c/y].

Kontogiannis, I., Tsiropoula, G., Tziotziou, K., et al. 2010, *Oscillations in a network region observed in the Hα line and their relation to the magnetic field*, A&A 524, A12, [15 c, 2 c/y].

Kosovichev, A.G. and Zharkova, V.V. 1998, *X-ray flare sparks quake inside Sun*, Nature 393, Issue 6683, [170 c, 9 c/y].

Kosovichev, A.G. 2007, *The cause of photospheric and helioseismic responses to solar flares: High-energy electrons or protons?* ApJ 670, L65, [28 c, 3 c/y].

Löhner-Böttcher, J. and Bello Gonzalez, N. 2015, *Signatures of running penumbral waves in sunspot photosphere*, A&A 580, A53, [12 c, 5 c/y].

Löhner-Böttcher, J., Bello Gonzalez, N., and Schmidt, W. 2016, *Magnetic field reconstruction based on sunspot oscillations*, Astron.Nachr. 337, 1040, [2 c, 1 c/y].

Martinez-Oliveros, J.C., Moradi, H., and Donea, A.C. 2008, *Seismic emissions from a highly impulsive M6.7 solar flare*, SoPh 251, 613, [20 c, 2 c/y].

Morton, R.J., Erdelyi, R., Jess, D.B., et al. 2011, *Observations of sausage modes in magnetic pores*, ApJL 729, L18, [40 c, 6 c/y].

Schrijver, C.J. and Brown, D.S. 2000, *Oscillations in the magnetic field of the solar corona in response to flares near the photosphere*, ApJ 537, L69, [71 c, 4 c/y].

Sharykin, I.N., Kosovichev, A.G., and Zimovets, I.V. 2015, *Energy release and initiation of a sunquake in a C-class flare*, ApJ 807, 102, [11 c, 4 c/y].

Sych, R., Nakariakov, V.M., Karlicky, M., et al. 2009, *Relationship between wave processes in sunspots and quasi-periodic pulsations in active region flares*, A&A 505, 791, [87 c, 10 c/y].

Tian, H., DeLuca, K.K., McKillop, S. et al. 2014, *High-resolution observations of the shock wave behavior for sunspot oscillations IRIS*, ApJ 786, 137, [48 c, 14 c/y].

Vecchio, A., Cauzzi, G., Reardon, K.P. et al. 2007, *Solar atmospheric oscillations and the chromospheric magnetic topology*, A&A 461, L1, [85 c, 8 c/y].

Zhao, J.W., Felipe, T., Chen, R., et al. 2016, *Tracing p-mode waves from the photosphere to the corona in active regions*, ApJ 830, L17, [6 c, 4 c/y].